

Standardizing reverberation-measured C IV time-lag quasars, and using them with standardized Mg II quasars to constrain cosmological parameters

Shulei Cao ¹★, Michal Zajaček ²†, Swayamtrupta Panda ^{3,4}‡§, Mary Loli Martínez-Aldama ⁵¶, Božena Czerny ³||, Bharat Ratra ¹★★

¹Department of Physics, Kansas State University, 116 Cardwell Hall, Manhattan, KS 66506, USA

²Department of Theoretical Physics and Astrophysics, Faculty of Science, Masaryk University, Kotlářská 2, 611 37 Brno, Czech Republic

³Center for Theoretical Physics, Polish Academy of Sciences, Al. Lotników 32/46, 02-668 Warsaw, Poland

⁴Laboratório Nacional de Astrofísica - MCTIC, R. dos Estados Unidos, 154 - Naçoes, Itajubá - MG, 37504-364, Brazil

⁵Departamento de Astronomía, Universidad de Chile, Camino del Observatorio 1515, Santiago, Chile

Accepted XXX. Received YYY; in original form ZZZ

ABSTRACT

We use 38 C IV quasar (QSO) reverberation-mapped (RM) observations, which span eight orders of magnitude in luminosity and the redshift range $0.001064 \leq z \leq 3.368$, to simultaneously constrain cosmological-model and QSO radius-luminosity ($R - L$) relation parameters in six cosmological models, using an improved technique that more correctly accounts for the asymmetric errors bars of the time-lag measurements. We find that $R - L$ relation parameters are independent of the cosmological models used in the analysis and so the $R - L$ relation can be used to standardize the C IV QSOs. The C IV QSO cosmological constraints are consistent with those from Mg II QSOs, allowing us to derive joint C IV + Mg II QSO cosmological constraints which are consistent with currently accelerated cosmological expansion, as well as consistent with cosmological constraints derived using better-established baryon acoustic oscillation (BAO) and Hubble parameter [$H(z)$] measurements. When jointly analyzed with $H(z)$ + BAO data, current C IV + Mg II QSO data mildly tighten current $H(z)$ + BAO data cosmological constraints.

Key words: cosmological parameters – dark energy – cosmology: observations – quasars: emission lines

1 INTRODUCTION

The well-established observed currently accelerated expansion of the Universe has motivated many theoretical cosmological models. In the standard general-relativistic spatially-flat Λ CDM cosmological model (Peebles 1984) dark energy in the form of a time-independent cosmological constant Λ powers the currently accelerated cosmological expansion and contributes $\sim 70\%$ of the current cosmological energy budget, with non-relativistic cold dark matter (CDM) and baryonic matter contributing $\sim 25\%$ and $\sim 5\%$, respectively. Although the flat Λ CDM model makes predictions consistent with most observations (see, e.g. Scolnic et al. 2018; Yu et al. 2018; Planck Collaboration 2020; eBOSS Collaboration 2021), it has some potential observational discrepancies (Di Valentino et al. 2021b; Perivolaropoulos & Skara 2022; Abdalla et al. 2022) that motivate us to also study dynamical dark energy models as well as models with non-zero spatial curvature.

There are better-established cosmological probes, such as baryon acoustic oscillation (BAO), type Ia supernova apparent magnitude, and Hubble parameter [$H(z)$] measurements that, when jointly analyzed, provide fairly restrictive cosmological parameter constraints (see, e.g. Cao & Ratra 2022). Cosmological probes that are now under active development can tighten these constraints. Amongst these developing probes are H II starburst galaxy apparent magnitude data that reach to redshift $z \sim 2.4$ (Mania & Ratra 2012; Chávez et al. 2014; González-Morán et al. 2021; Cao et al. 2020, 2021b; Johnson et al. 2022; Mehrabi et al. 2022), quasar (QSO) angular size measurements that reach to $z \sim 2.7$ (Cao et al. 2017; Ryan et al. 2019; Zheng et al. 2021; Lian et al. 2021; Cao et al. 2022b), QSO flux observations that reach to $z \sim 7.5$ (Risaliti & Lusso 2015, 2019; Khadka & Ratra 2020a,b, 2021, 2022; Lusso et al. 2020; Zhao & Xia 2021; Rezaei et al. 2022; Luongo et al. 2022; Leizerovich et al. 2022; Colgáin et al. 2022; Dainotti et al. 2022b),¹ gamma-ray burst data that reach to $z \sim 8.2$ (Wang et al. 2016, 2022; Fana Dirirsa et al. 2019; Demianski et al. 2021; Khadka & Ratra 2020c; Hu et al. 2021;

★ E-mail: shulei@phys.ksu.edu

† E-mail: zajacek@mail.muni.cz

‡ E-mail: panda@cft.edu.pl

§ CNPq Fellow

¶ E-mail: mmartinez@das.uchile.cl

|| E-mail: bcz@cft.edu.pl

★★ E-mail: ratra@phys.ksu.edu

¹ Note however that the Lusso et al. (2020) QSO flux compilation assumes a model for the QSO UV–X-ray correlation that is invalid above redshifts $z \sim 1.5 - 1.7$ so this is the limit to which the Lusso et al. (2020) QSOs can be used to determine cosmological constraints (Khadka & Ratra 2021, 2022).

Khadka et al. 2021b; Luongo & Muccino 2021; Cao et al. 2021a, 2022a,c,d; Dainotti et al. 2022a; Liu et al. 2022), and — the main subject of our paper — reverberation-mapped (RM) QSO data that reach to $z \sim 3.4$ (Czerny et al. 2021; Zajaček et al. 2021; Khadka et al. 2021a; Khadka et al. 2022b; Khadka et al. 2022a, and this paper).

Khadka et al. (2021a); Khadka et al. (2022b); Khadka et al. (2022a) derived cosmological constraints from RM H β and Mg II QSO data. In this paper, we show that RM C IV QSO data, that extend to higher z , are standardizable and derive the first cosmological constraints from C IV data.

With its ionization potential energy of ~ 64.5 eV, C IV ($\lambda 1549$) belongs to the high-ionization line (HIL) component of the QSO broad-line region (BLR; Collin-Souffrin et al. 1988; Baskin & Laor 2005; Karas et al. 2021), which can partially form an outflow that is manifested by the blueshifted centroid of the line (see e.g. Britzen et al. 2021) as well as by the frequent blueward line-emission asymmetry (Baskin & Laor 2005). It is therefore not yet established whether all of the C IV material is virialized and if the standard reverberation mapping (hereafter RM²) of HILs can lead to the reliable measurements of the SMBH masses, as was previously done using the low-ionization lines (LILs) for several hundreds of objects (mainly using the Balmer line H β and the resonance Mg II line).

However, the BLR radius-luminosity ($R - L$) relationship for the C IV line, in the flat Λ CDM model, appears to now be well established with a significant positive correlation and a relatively small dispersion (Kaspi et al. 2007; Lira et al. 2018; Grier et al. 2019; Kaspi et al. 2021), which allows for the possibility of using this relation for constraining cosmological parameters as we previously did for H β and Mg II lines (Martínez-Aldama et al. 2019; Panda et al. 2019a; Zajaček et al. 2021; Czerny et al. 2021; Khadka et al. 2021a; Khadka et al. 2022b; Khadka et al. 2022a).

In this paper, we use 38 high-quality C IV QSO measurements, which span eight orders of magnitude in luminosity $\sim 10^{40-48}$ erg s⁻¹ and the redshift range $0.001064 \leq z \leq 3.368$, to constrain, for the first time, cosmological-model and $R - L$ relation parameters, in six general relativistic dark energy cosmological models, using a more correct technique to account for the asymmetric errors of the time-lag measurements. We find that the C IV $R - L$ relation parameters are independent of cosmological model, so C IV QSO data are standardizable through the C IV $R - L$ relation. Mg II QSO data were also found to be standardizable through the Mg II $R - L$ relation (Khadka et al. 2021a; Khadka et al. 2022b). We find that cosmological constraints from C IV and Mg II QSO data are mutually consistent and are also consistent with those from $H(z) +$ BAO data. Although the cosmological constraints from the joint analysis of C IV + Mg II QSO data are weak, jointly analyzing C IV + Mg II data with $H(z) +$ BAO data results in a mild ($< 0.1\sigma$) tightening of the $H(z) +$ BAO cosmological constraints.

This paper is organized as follows. We briefly introduce the cosmological models/parametrizations we study in Section 2. In Sections 3 and 4, we outline the data sets and the analysis methods we use, respectively. Our constrained cosmological parameter and $R - L$ relation parameter results are presented and discussed in Sections 5 and 6. We summarize our conclusions in Section 7.

² Depending on the context, we use the abbreviation RM for both reverberation mapping as a method and for reverberation-mapped quasars interchangeably.

2 COSMOLOGICAL MODELS

We use various combinations of data to simultaneously constrain cosmological model parameters and C IV and Mg II QSO $R - L$ relation parameters in six spatially-flat and non-flat dark energy cosmological models.³ The Hubble parameter $H(z)$, discussed below, is used to make theoretical predictions in these cosmological models.

In the cosmological models here, we assume one massive and two massless neutrino species with the non-relativistic neutrino physical energy density parameter $\Omega_\nu h^2 = \sum m_\nu / (93.14 \text{ eV}) = 0.06 \text{ eV} / (93.14 \text{ eV})$, where h is the Hubble constant H_0 in units of $100 \text{ km s}^{-1} \text{ Mpc}^{-1}$. The non-relativistic matter density parameter $\Omega_{m0} = (\Omega_\nu h^2 + \Omega_b h^2 + \Omega_c h^2) / h^2$, where $\Omega_b h^2$ and $\Omega_c h^2$ are the current values of the observationally-constrained baryonic and cold dark matter physical energy density parameters, respectively.⁴ Including neutrino species is more accurate even though it only has a mild effect on the constraints from Mg II and C IV data.

In the Λ CDM models the Hubble parameter

$$H(z, \mathbf{p}) = H_0 \sqrt{\Omega_{m0} (1+z)^3 + \Omega_{k0} (1+z)^2 + \Omega_\Lambda}, \quad (1)$$

where the cosmological parameters $\mathbf{p} = \{\Omega_{k0}, \Omega_{m0}, H_0\}$ with Ω_{k0} being the spatial curvature energy density parameter and the cosmological constant dark energy density parameter $\Omega_\Lambda = 1 - \Omega_{m0} - \Omega_{k0}$. In the flat Λ CDM model the constrained cosmological parameters are H_0 , $\Omega_b h^2$, and $\Omega_c h^2$ (only Ω_c is constrained in the C IV QSO and Mg II QSO alone cases), whereas in the non-flat Λ CDM model one additional cosmological parameter, Ω_{k0} , is constrained.

In the XCDM parametrizations

$$H(z, \mathbf{p}) = H_0 \sqrt{\Omega_{m0} (1+z)^3 + \Omega_{k0} (1+z)^2 + \Omega_{X0} (1+z)^{3(1+w_X)}}, \quad (2)$$

where the cosmological parameters $\mathbf{p} = \{\Omega_{k0}, \Omega_{m0}, H_0, w_X\}$ with w_X being the X-fluid equation of state parameter ($w_X = -1$ correspond to Λ CDM models). The current value of the dynamical dark energy density parameter of the X-fluid $\Omega_{X0} = 1 - \Omega_{m0} - \Omega_{k0}$. In the flat XCDM parameterization the constrained cosmological parameters are H_0 , $\Omega_b h^2$, $\Omega_c h^2$, and w_X (only Ω_c and w_X are constrained in the C IV QSO and Mg II QSO alone cases), whereas in the non-flat XCDM parameterization Ω_{k0} is constrained as well.

In the ϕ CDM models (Peebles & Ratra 1988; Ratra & Peebles 1988; Pavlov et al. 2013)⁵

$$H(z, \mathbf{p}) = H_0 \sqrt{\Omega_{m0} (1+z)^3 + \Omega_{k0} (1+z)^2 + \Omega_\phi(z, \alpha)}, \quad (3)$$

where the cosmological parameters $\mathbf{p} = \{\Omega_{k0}, \Omega_{m0}, H_0, \alpha\}$ and the

³ For discussions of spatial curvature observational constraints see Chen et al. (2016), Rana et al. (2017), Ooba et al. (2018a,c), Park & Ratra (2019c,a), DES Collaboration (2019), Li et al. (2020), Handley (2019), Efstathiou & Gratton (2020), Di Valentino et al. (2021a), Vagnozzi et al. (2021a,b), KiDS Collaboration (2021), Arjona & Nesseris (2021), Dhawan et al. (2021), Renzi et al. (2022), Geng et al. (2022), Wei & Melia (2022), Mukherjee & Banerjee (2022), Glanville et al. (2022), and references therein.

⁴ In the C IV QSO and Mg II QSO alone cases, the current value of the baryonic matter energy density parameter and the Hubble constant are set to $\Omega_b = 0.05$ and $H_0 = 70 \text{ km s}^{-1} \text{ Mpc}^{-1}$, respectively, because these data alone are unable to constrain Ω_b and H_0 .

⁵ For discussions of ϕ CDM observational constraints see Zhai et al. (2017), Ooba et al. (2018b, 2019), Park & Ratra (2018, 2019b, 2020), Solà Peracaula et al. (2019), Singh et al. (2019), Ureña-López & Roy (2020), Sinha & Banerjee (2021), Xu et al. (2022), de Cruz Perez et al. (2021), Jesus et al. (2021), and references therein.

scalar field, ϕ , dynamical dark energy density parameter,

$$\Omega_\phi(z, \alpha) = \frac{1}{6H_0^2} \left[\frac{1}{2} \dot{\phi}^2 + V(\phi) \right], \quad (4)$$

is determined by numerically solving the Friedmann equation (3) and the equation of motion of the scalar field

$$\ddot{\phi} + 3H\dot{\phi} + V'(\phi) = 0. \quad (5)$$

Here we assume an inverse power-law scalar field potential energy density

$$V(\phi) = \frac{1}{2} \kappa m_p^2 \phi^{-\alpha}. \quad (6)$$

In these equations, an overdot and a prime denote a derivative with respect to time and ϕ , respectively, m_p is the Planck mass, α is a positive constant ($\alpha = 0$ correspond to Λ CDM models), and κ is a constant that is determined by the shooting method implemented in the Cosmic Linear Anisotropy Solving System (CLASS) code (Blas et al. 2011). In the flat ϕ CDM model the constrained cosmological parameters are H_0 , $\Omega_b h^2$, $\Omega_c h^2$, and α (only Ω_c and α are constrained in the C iv QSO and Mg II QSO alone cases), whereas in the non-flat ϕ CDM model Ω_{k0} is also constrained.

3 DATA

In this work, we use C iv QSO, Mg II QSO, and $H(z) + \text{BAO}$ data, as well as combinations of these data sets, to constrain cosmological-model and QSO $R - L$ relation parameters. These data sets are summarized next, with the emphasis on the C iv QSO sample.

C iv QSO data. Here we describe the sample of high-quality 38 C iv RM QSOs. The first time-lag measurements of the broad C iv line were inferred by Peterson et al. (2005, 2006) for 4 sources. The source NGC4151 was monitored by Metzroth et al. (2006). The C iv time-lag for the intensively monitored NGC5548 was determined by De Rosa et al. (2015). Lira et al. (2018) performed RM for 17 high-luminosity QSOs for over 10 years, out of which 8 QSOs were reported to have statistically significant ($> 1\sigma$) C iv time-lag measurements. Hoormann et al. (2019) report 2 C iv detections for quasars at $z = 1.905$ and $z = 2.593$ from the photometric Dark Energy Survey Supernova Program (DES-SN) and the spectroscopic Australian Dark Energy Survey (Oz-DES). Within the Sloan Digital Sky Survey Reverberation Mapping project (SDSS-RM), Grier et al. (2019) determined C iv time-lag measurements for 48 QSOs with an average false-positive rate of 10%. Of these, 16 QSOs pass the highest-quality criteria, in the redshift range of $1.4 < z < 2.8$ and the monochromatic luminosity range $44.5 < \log [L_{1350} (\text{erg s}^{-1})] < 45.6$. Shen et al. (2019) showed that adding more photometric data points and spectroscopic data (9 + 5 years of photometric and spectroscopic measurements, respectively, in comparison to 4 + 4 years of spectroscopic and photometric monitoring performed by Grier et al., 2019) results in the significant detection of 3 more C iv time-lag measurements. Using 20 years of photometric and spectrophotometric data, Kaspi et al. (2021) report significant C iv time-delays for 3 QSOs at redshifts $z = 2.172$, 2.646 , and 3.192 .

Kaspi et al. (2021) compiled (with a few corrections) available C iv RM sources, finding 38 QSOs with significantly measured C iv time-delays, including their 3 QSOs. The time-delays were determined by using either the interpolated cross-correlation function (ICCF) or the z -transformed discrete correlation function (zDCF) or a combination

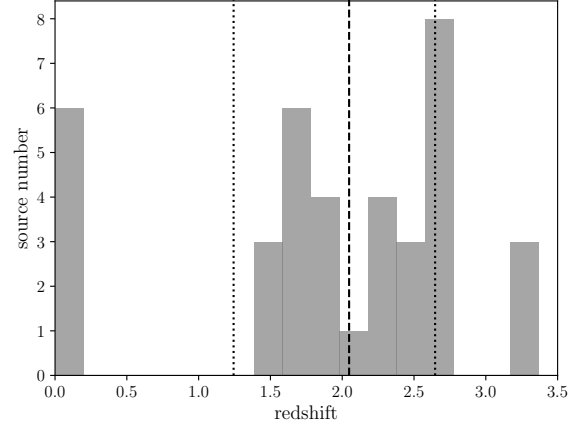


Figure 1. The redshift distribution for the “golden” sample of 38 C iv QSOs from Kaspi et al. (2021). The dashed line stands for the redshift median at 2.048, while the dotted lines represent 16% and 84% percentiles at 1.244 and 2.647, respectively. The histogram bin size is $\Delta z \approx 0.2$.

of both, which ensures a relative homogeneity of the sample in terms of the time-delay methodology in comparison with, e.g., the H β sample where several different methods are applied and combined, see e.g. Zajaček et al. (2019) or Rakshit (2020) for overviews. We refer to this sample of 38 C iv QSOs as “golden” and it covers the redshift range $0.001064 \leq z \leq 3.368$, with the median redshift of 2.048 and 16-% and 84-% percentile redshifts of 1.244 and 2.647, respectively. The redshift distribution is shown in Fig. 1. The sources belonging to the golden sample are listed in Table A1, including their redshift, flux density at 1350 Å, monochromatic luminosity at 1350 Å (computed assuming a flat Λ CDM model with $H_0 = 70 \text{ km s}^{-1} \text{ Mpc}^{-1}$, $\Omega_{m0} = 0.3$, and $\Omega_\Lambda = 0.7$), and the rest-frame C iv time-lag τ (typically with asymmetrical error bars).

The correlation between the rest-frame C iv time-delay and the UV monochromatic luminosity at 1350 Å is significant, with the Pearson correlation coefficient $r = 0.898$ ($p = 2.082 \times 10^{-14}$) and the Spearman rank-order correlation coefficient $s = 0.799$ ($p = 1.751 \times 10^{-9}$). Given the large correlation coefficient, we fit the golden dataset with the power-law relation $\log \tau = \beta_C + \gamma_C \log (L_{1350}/10^{44} \text{ erg s}^{-1})$, where $\log \equiv \log_{10}$, and find the best-fit intercept $\beta_C = 1.04 \pm 0.07$ and the best-fit slope $\gamma_C = 0.42 \pm 0.03$, for which the individual time-delay errors were neglected in the Levenberg-Marquardt algorithm. This results in an intrinsic scatter of $\sigma = 0.32$ dex and $\chi^2 = 31.8$ (36 degrees of freedom). When we consider individual symmetrized time-delay errors (see the discussion in the paragraph below eq. (18)), we obtain $\gamma_C = 0.56 \pm 0.04$ and $\beta_C = 0.98 \pm 0.07$ with $\sigma = 0.41$ dex and $\chi^2 = 16.6$. See Fig. 2 for the best-fitting relations, which were inferred using the `curve_fit` function from the `scipy` library. To add information about the accretion state of each QSO from our sample in the $R - L$ relation, we estimate the Eddington ratio $\lambda_{\text{Edd}} = L_{\text{bol}}/L_{\text{Edd}}$, where $L_{\text{bol}} = \kappa_{\text{bol}} L_{1350}$ is the bolometric luminosity calculated using the luminosity-dependent bolometric factor κ_{bol} according to Netzer (2019), and L_{Edd} is the Eddington luminosity (Zajaček et al. 2014; Eckart et al. 2017; Zajaček et al. 2020b). To obtain L_{Edd} , the supermassive black hole (SMBH) mass was calculated using the virial relation $M_\bullet = f_{\text{vir}} c \tau \text{FWHM}^2 / G$, where the virial factor f_{vir} was estimated using the fitted formula that inversely scales with the full width at half maximum, FWHM, see Mejía-Restrepo et al. (2018). The FWHM and τ values were

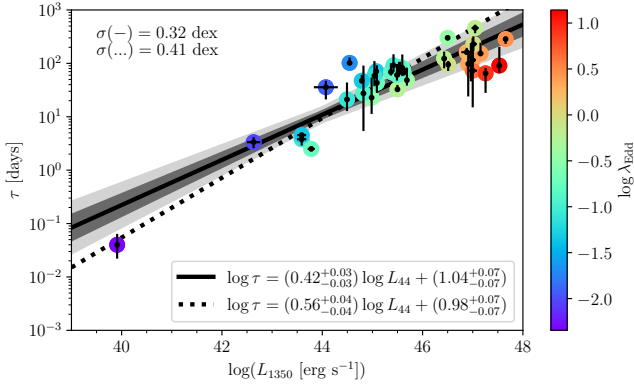


Figure 2. Radius-luminosity relationship for the “golden” sample of 38 C IV QSOs (see also Kaspi et al. 2021). The luminosity at 1350 Å is based on the flat Λ CDM model (with $H_0 = 70 \text{ km s}^{-1} \text{ Mpc}^{-1}$, $\Omega_{m0} = 0.3$, and $\Omega_{\Lambda} = 0.7$). The points are colour-coded with respect to the calculated Eddington ratio $\lambda_{\text{Edd}} = L_{\text{bol}}/L_{\text{Edd}}$ of the source. When we neglect individual time-delay errors, the best-fit relation (black solid line) determined by the Levenberg-Marquardt algorithm has a slope of $\gamma_C = 0.42 \pm 0.03$ and a scatter of $\sigma = 0.32$ dex. The dark and light gray areas around the best-fit solid line are one and two sigma confidence regions. Considering individual time-delay errors yields the best-fit relation (dotted line) with a larger slope of $\gamma_C = 0.56 \pm 0.04$ and the scatter of data around this relation is $\sigma = 0.41$ dex.

adopted from the compilation of Kaspi et al. (2021). In Fig. 2 each source is coloured by the corresponding value of $\log \lambda_{\text{Edd}}$.

Apart from the “golden” C IV AGN sample reported by Kaspi et al. (2021), there are additional lower-quality C IV time-lag detections reported in literature. Grier et al. (2019) report additional 32 C IV detections with a lower quality rating of 1, 2, and 3.⁶ As a follow-up of the Oz-DES RM project, Penton et al. (2022) designed a quality-cut methodology and out of 6 test sources, 2 at redshifts 1.93 and 2.74 pass all the quality criteria. These additional 34 sources will be considered in a future study.

Mg II QSO data. As listed in table A1 of Khadka et al. (2021a), the Mg II QSO sample consists of 78 QSOs and spans the redshift range $0.0033 \leq z \leq 1.89$. Detailed descriptions of Mg II QSO data can be found in Khadka et al. (2021a) and Martínez-Aldama et al. (2020b), where it was shown that they obey the $R - L$ relation, with measured quantities being time-delay τ' and QSO flux F_{3000} measured at 3000 Å; see also Prince et al. (2022) for an updated Mg II QSO $R - L$ relation in the fixed flat Λ CDM cosmology. We note that the Mg II QSO sample is relatively homogeneous since 57 significant time-delay detections (hence 73% of Mg II QSO sources) were determined by Homayouni et al. (2020), who applied a consistent time-delay method to all the sources based on JAVELIN (Zu et al. 2011), which was compared with the CREAM results that were generally consistent (Starkey et al. 2016). However, the time-delay uncertainties for this sample are not completely homogeneous and a consistent treatment of the continuum and the line-emission light-curve correlation and the time-delay inference is needed to homogenize the sample of the best Mg II QSO time delays and their uncertainties.

⁶ Grier et al. (2019) assign the quality flag of 1 to the lowest-quality time-lag detections, while 5 is the highest quality rating. There are different factors considered in the rating scheme, such as the clear correlation between the continuum and C IV emission-line light curves, overall consistency between JAVELIN, CREAM, and ICCF time-lag detections, and the presence of multiple significant time-lag peaks.

$H(z) + \text{BAO data}$. There are 32 $H(z)$ and 12 BAO measurements listed in Tables 1 and 2 of Cao & Ratra (2022), spanning the redshift ranges $0.07 \leq z \leq 1.965$ and $0.122 \leq z \leq 2.334$, respectively.

4 DATA ANALYSIS METHODOLOGY

We utilize the $R - L$ relation parametrization according to Bentz et al. (2013), where we replace the monochromatic luminosity and rest-frame time-delay taking into account the C IV-region emission properties

$$\log \frac{\tau}{\text{days}} = \beta_C + \gamma_C \log \frac{L_{1350}}{10^{44} \text{ erg s}^{-1}}, \quad (7)$$

where τ , β_C , and γ_C are the C IV time-lag, the intercept parameter, and the slope parameter, respectively, and the monochromatic luminosity at 1350 Å

$$L_{1350} = 4\pi D_L^2 F_{1350}, \quad (8)$$

with measured quasar flux F_{1350} at 1350 Å in units of $\text{erg s}^{-1} \text{ cm}^{-2}$. The luminosity distance is a function of redshift z and the cosmological parameters,

$$D_L(z) = \begin{cases} \frac{c(1+z)}{H_0 \sqrt{\Omega_{k0}}} \sinh \left[\frac{H_0 \sqrt{\Omega_{k0}}}{c} D_C(z) \right] & \text{if } \Omega_{k0} > 0, \\ (1+z) D_C(z) & \text{if } \Omega_{k0} = 0, \\ \frac{c(1+z)}{H_0 \sqrt{|\Omega_{k0}|}} \sin \left[\frac{H_0 \sqrt{|\Omega_{k0}|}}{c} D_C(z) \right] & \text{if } \Omega_{k0} < 0, \end{cases} \quad (9)$$

where the comoving distance is

$$D_C(z) = c \int_0^z \frac{dz'}{H(z')}, \quad (10)$$

with c being the speed of light.

The Mg II QSO $R - L$ relation is

$$\log \frac{\tau'}{\text{days}} = \beta_M + \gamma_M \log \frac{L_{3000}}{10^{44} \text{ erg s}^{-1}}, \quad (11)$$

where τ' , β_M , and γ_M are the Mg II time-lag, the intercept parameter, and the slope parameter, respectively, and the monochromatic luminosity at 3000 Å

$$L_{3000} = 4\pi D_L^2 F_{3000}, \quad (12)$$

with measured quasar flux F_{3000} at 3000 Å in units of $\text{erg s}^{-1} \text{ cm}^{-2}$.

The natural log of the C IV likelihood function (D’Agostini 2005) is

$$\ln \mathcal{L}_{\text{C IV}} = -\frac{1}{2} \left[\chi_{\text{C IV}}^2 + \sum_{i=1}^N \ln \left(2\pi \sigma_{\text{tot},c,i}^2 \right) \right], \quad (13)$$

where

$$\chi_{\text{C IV}}^2 = \sum_{i=1}^N \left[\frac{(\log \tau_{\text{obs},i} - \beta_C - \gamma_C \log L_{1350,i})^2}{\sigma_{\text{tot},c,i}^2} \right] \quad (14)$$

with total uncertainty

$$\sigma_{\text{tot},c,i}^2 = \sigma_{\text{int},c}^2 + \sigma_{\log \tau_{\text{obs},i}}^2 + \gamma_C^2 \sigma_{\log F_{1350,i}}^2, \quad (15)$$

where $\sigma_{\text{int},c}$ is the C IV QSO intrinsic scatter parameter which also contains the unknown systematic uncertainty, and N is the number of data points.

Table 1. Flat priors of the constrained parameters.

Parameter	Prior
Cosmological-Model Parameters	
H_0 ^a	[None, None]
$\Omega_b h^2$ ^b	[0, 1]
$\Omega_c h^2$ ^c	[0, 1]
Ω_{k0}	[-2, 2]
α	[0, 10]
w_X	[-5, 0.33]
$R - L$ Relation Parameters	
γ	[0, 5]
β	[0, 10]
σ_{int}	[0, 5]

^a $\text{km s}^{-1} \text{Mpc}^{-1}$. In the C iv QSO and Mg II QSO alone cases, H_0 is set to be $70 \text{ km s}^{-1} \text{Mpc}^{-1}$, while in other cases, the prior range is irrelevant (unbounded).

^b In the C iv QSO and Mg II QSO alone cases, $\Omega_b h^2$ is set to be 0.0245, i.e. $\Omega_b = 0.05$.

^c In the C iv QSO and Mg II QSO alone cases, $\Omega_{m0} \in [0, 1]$ is ensured.

The natural log of the Mg II likelihood function is

$$\ln \mathcal{L}_{\text{Mg II}} = -\frac{1}{2} \left[\chi_{\text{Mg II}}^2 + \sum_{i=1}^N \ln \left(2\pi\sigma_{\text{tot},i}^2 \right) \right], \quad (16)$$

where

$$\chi_{\text{Mg II}}^2 = \sum_{i=1}^N \left[\frac{(\log \tau'_{\text{obs},i} - \beta_M - \gamma_M \log L_{3000,i})^2}{\sigma_{\text{tot},i}^2} \right] \quad (17)$$

with total uncertainty

$$\sigma_{\text{tot},i}^2 = \sigma_{\text{int},M}^2 + \sigma_{\log \tau'_{\text{obs},i}}^2 + \gamma_M^2 \sigma_{\log F_{3000,i}}^2, \quad (18)$$

where $\sigma_{\text{int},M}$ is the Mg II QSO intrinsic scatter parameter which also contains the unknown systematic uncertainty.

The τ error bars are typically asymmetric. As used for Mg II QSOs in Khadka et al. (2021a) and Cao & Ratra (2022), in what follows, τ symmetrized errors mean that we are using symmetrized σ_τ 's defined as $\sigma_\tau = [2\sigma_{\tau,+}\sigma_{\tau,-}/(\sigma_{\tau,+} + \sigma_{\tau,-}) + \sqrt{\sigma_{\tau,+}\sigma_{\tau,-}}]/2$, where $\sigma_{\tau,+}$ and $\sigma_{\tau,-}$ are the upper and lower errors of τ , respectively. On the other hand, τ asymmetric errors mean that we directly use asymmetric $\sigma_{\tau,+}$ and $\sigma_{\tau,-}$ as follows: when the theoretical prediction for $\log \tau$ is larger (smaller) than the observed value, $\sigma_\tau = \sigma_{\tau,+}$ ($\sigma_\tau = \sigma_{\tau,-}$).

The detailed descriptions for the likelihood functions of $H(z)$ and BAO data can be found in Cao et al. (2020).

We list the flat priors of the free cosmological-model and $R - L$ relation parameters in Table 1. By maximizing the likelihood functions, we obtain the unmarginalized best-fitting values and posterior distributions of all free cosmological-model and $R - L$ relation parameters. The Markov chain Monte Carlo (MCMC) code MONTEPYTHON (Audren et al. 2013; Brinckmann & Lesgourgues 2019), the CLASS code, and the PYTHON package GETDIST (Lewis 2019) are used to perform our analyses.

One can find the definitions of the Akaike Information Criterion (AIC), the Bayesian Information Criterion (BIC), and the Deviance Information Criterion (DIC) in our previous paper (see, e.g. Cao et al. 2022d). ΔAIC , ΔBIC , and ΔDIC are computed as the differences between the AIC, BIC, and DIC values of the other five cosmological

dark energy models and those of the flat ΛCDM reference model. Positive (negative) values of these ΔICs show that the model under investigation fits the data worse (better) than does the flat ΛCDM reference model. In comparison with the model with the minimum IC, $\Delta\text{IC} \in (0, 2]$ indicates weak evidence against the model under investigation, $\Delta\text{IC} \in (2, 6]$ indicates positive evidence against the model under investigation, $\Delta\text{IC} \in (6, 10]$ indicates strong evidence against the model under investigation, and $\Delta\text{IC} > 10$ indicates very strong evidence against the model under investigation.

5 RESULTS

The posterior one-dimensional probability distributions and two-dimensional confidence regions of cosmological-model and $R - L$ relation parameters for the six cosmological models are shown in Figs. 3–8, where in panel (a) of each figure results of the C iv data analyses with symmetrized errors and asymmetric errors are shown in green and red, respectively; in panel (b) of each figure results of the Mg II data analyses with symmetrized errors and asymmetric errors are shown in green and red, respectively; in panel (c) of each figure the results of the C iv, Mg II, and joint C iv + Mg II data analyses with asymmetric errors, and the $H(z) + \text{BAO}$ data analysis are shown in red, green, blue, and black, respectively; and in panels (d) and (e) of each figure the results of the joint (asymmetric errors) C iv + Mg II, $H(z) + \text{BAO}$, and $H(z) + \text{BAO} + \text{C iv} + \text{Mg II}$ data analyses are shown in grey, blue, and red, respectively. The unmarginalized best-fitting parameter values, as well as the values of maximum likelihood \mathcal{L}_{max} , AIC, BIC, DIC, ΔAIC , ΔBIC , and ΔDIC , for all models and data sets, are listed in Table 2. The marginalized posterior mean parameter values and uncertainties ($\pm 1\sigma$ error bars and 1 or 2σ limits), for all models and data sets, are listed in Table 3.

In all six cosmological models, all data combinations more favour currently accelerating cosmological expansion. This is also the case with Mg II QSO data (Khadka et al. 2021a; Khadka et al. 2022b), but differs from what happens with H β QSO data, which more favour currently decelerated cosmological expansion (Khadka et al. 2022a).

5.1 Constraints from C iv, Mg II, and C iv + Mg II QSO data

As shown in panels (a) and (b) of Figs. 3–8 and Table 3, we find that results from C iv QSO and Mg II QSO symmetrized errors data analyses are only mildly different (less than 1σ) from those of C iv QSO and Mg II QSO asymmetric errors data analyses. Since the analyses with asymmetric errors are the more correct ones, we summarize the asymmetric errors C iv results in what follows. The symmetric errors Mg II results are discussed in Khadka et al. (2021a).

The Ω_{m0} constraints from C iv data range from a low of < 0.840 (2σ , flat XCDM) to a high of $0.467^{+0.199}_{-0.378}$ (1σ , non-flat ΛCDM).

The Ω_{k0} constraints from C iv data are $-0.330^{+0.534}_{-1.060}$, $-0.168^{+0.451}_{-0.789}$, and $0.096^{+0.359}_{-0.337}$ for non-flat ΛCDM , XCDM, and ϕCDM , respectively. Although C iv data favour closed hypersurfaces in non-flat ΛCDM and non-flat XCDM, and favour open hypersurfaces in non-flat ϕCDM , flat hypersurfaces are well within 1σ . C iv data only provide very weak constraints of w_X and α .

From panels (c) of Figs. 3–8, we see that the cosmological-model parameter constraints from C iv QSO data and from Mg II QSO data are mutually consistent, as are the cosmological constraints from C iv QSO and $H(z) + \text{BAO}$ data and from Mg II QSO and $H(z) +$

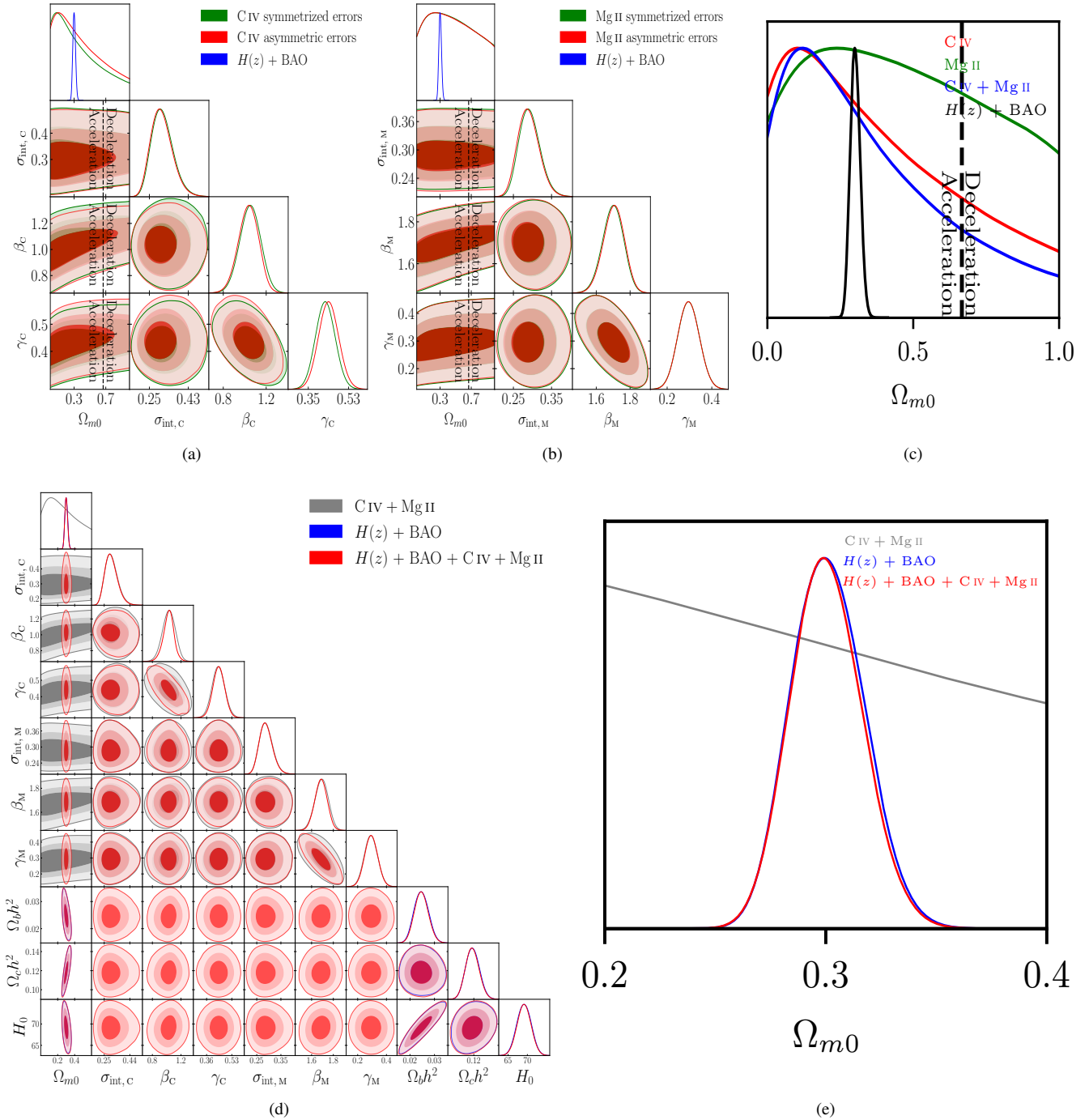


Figure 3. One-dimensional likelihood distributions and 1σ , 2σ , and 3σ two-dimensional likelihood confidence contours for flat Λ CDM from various combinations of data. The zero-acceleration black dashed lines in panels (a) and (b) divide the parameter space into regions associated with currently-accelerating (left) and currently-decelerating (right) cosmological expansion.

BAO data.⁷ It is therefore reasonable to perform joint analyses of C IV QSO and Mg II QSO data. As shown in panels (d) and (e) of

⁷ Khadka et al. (2021a); Khadka et al. (2022b) had earlier shown that the symmetric errors Mg II cosmological constraints are mutually consistent with those from $H(z) + \text{BAO}$ data. This differs from the H β QSOs cosmological constraints, which are $\sim 2\sigma$ inconsistent with those from $H(z) + \text{BAO}$ data (Khadka et al. 2022a).

Figs. 3–8, the cosmological-model parameter constraints from C IV + Mg II QSO data and from $H(z) + \text{BAO}$ data are mutually consistent at $\lesssim 1.5\sigma$,⁸ so these data sets can be jointly analyzed.

The constraints on the C IV $R - L$ relation parameters in the six different cosmological models are mutually consistent, so the $R - L$

⁸ I.e., in the two-dimensional contour plots all or most of the 1σ $H(z) + \text{BAO}$ data contour always lie inside the 2σ C IV + Mg II QSO data contour.

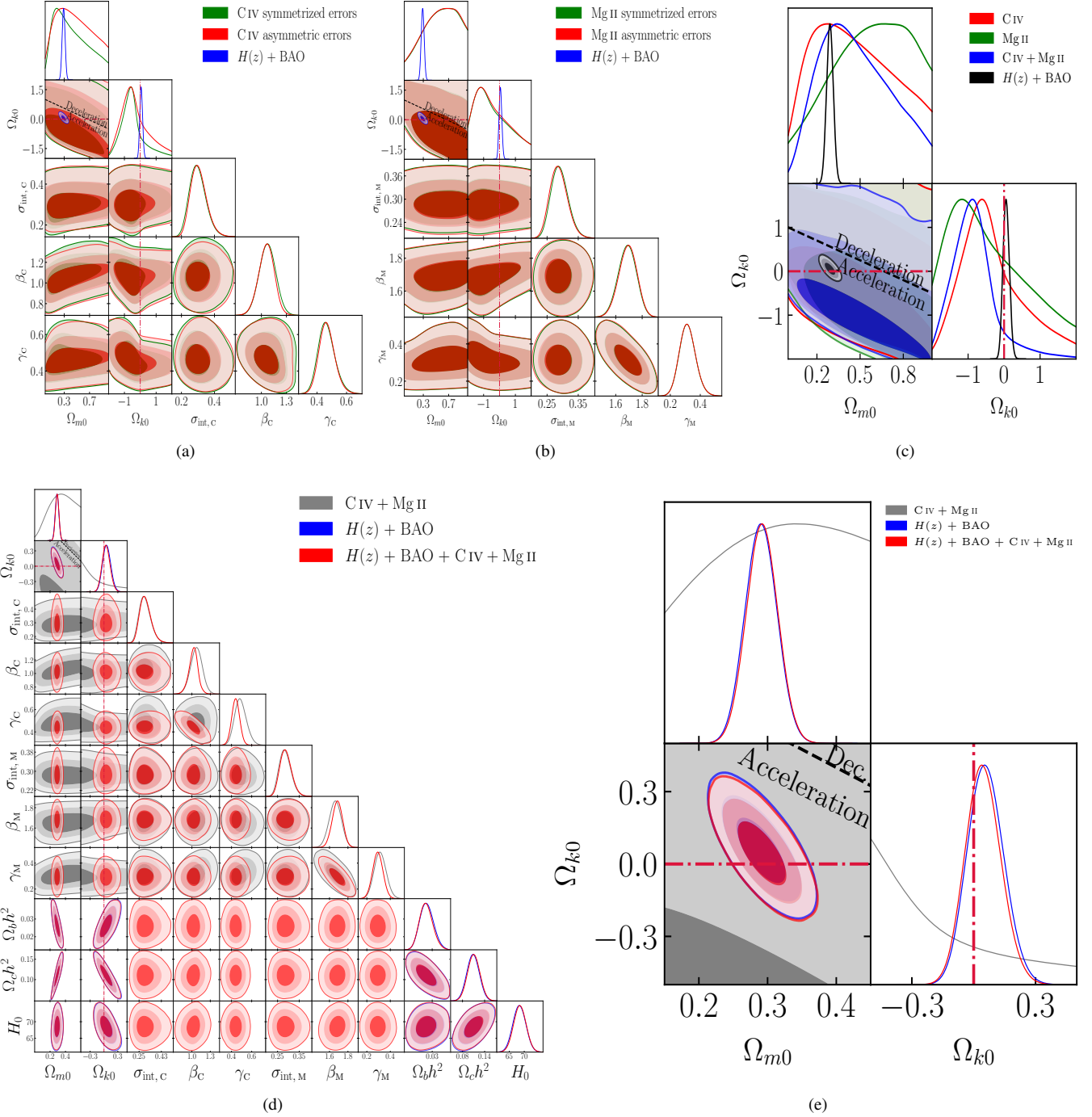


Figure 4. Same as Fig. 3 but for non-flat ΛCDM . The zero-acceleration black dashed lines divide the parameter space into regions associated with currently-accelerating (below left) and currently-decelerating (above right) cosmological expansion.

relation CIV data set is standardizable. The constraints on the intrinsic scatter parameter of the CIV $R - L$ relation, $\sigma_{\text{int},c}$, range from a low of $0.296^{+0.041}_{-0.056}$ (flat XCDM) to a high of $0.314^{+0.038}_{-0.055}$ (flat ϕCDM), with a difference of 0.26σ , which are $\sim 0.1 - 0.4\sigma$ larger than those of Mg II ($\sigma_{\text{int},m}$). The constraints on the slope parameter of the CIV $R - L$ relation, γ_c , range from a low of 0.426 ± 0.049 (flat XCDM) to a high of $0.468^{+0.046}_{-0.056}$ (non-flat ΛCDM), with a difference of 0.56σ . The constraints on the intercept parameter of the CIV $R - L$

relation, β_c , range from a low of $0.970^{+0.136}_{-0.108}$ (flat XCDM) to a high of $1.076^{+0.087}_{-0.074}$ (non-flat ϕCDM), with a difference of 0.68σ .

A summary value of the measured CIV $R - L$ relation slope, $\gamma_c \simeq 0.45 \pm 0.04$, indicates that it is about 1σ lower than and consistent with the prediction of simple photoionization theory ($\gamma = 0.5$, Karas et al. 2021; Panda 2022), on the other hand a summary value of the measured Mg II $R - L$ relation slope, $\gamma_m \simeq 0.3 \pm 0.05$ (also see Khadka et al. 2021a; Khadka et al. 2022b), indicates that it is about 4σ lower than $\gamma = 0.5$.

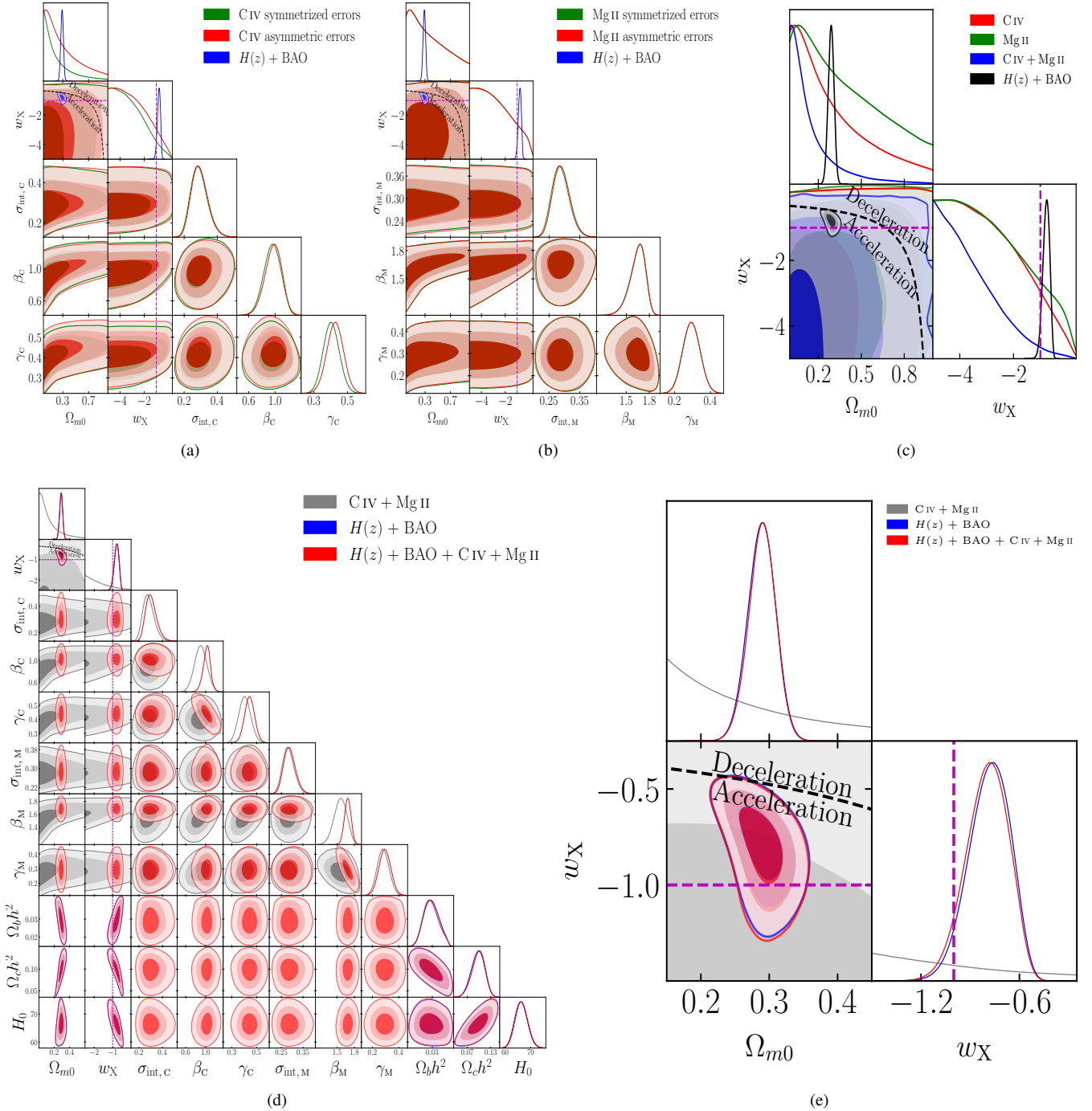


Figure 5. One-dimensional likelihood distributions and 1σ , 2σ , and 3σ two-dimensional likelihood confidence contours for flat XCDM from various combinations of data. The zero-acceleration black dashed lines divide the parameter space into regions associated with currently-accelerating (either below left or below) and currently-decelerating (either above right or above) cosmological expansion. The magenta dashed lines represent $w_X = -1$, i.e. flat Λ CDM.

The Ω_{m0} constraints from (asymmetric errors) C IV + Mg II data range from a low of < 0.563 (2σ , flat XCDM) to a high of < 0.537 (1σ , flat ϕ CDM).

The Ω_{k0} constraints from C IV + Mg II data are $-0.818^{+0.391}_{-0.637}$ (< 0.474 , 2σ), $-0.410^{+0.368}_{-0.222}$ ($-0.410^{+0.698}_{-0.846}$, 2σ), and $0.088^{+0.384}_{-0.364}$ ($0.088^{+0.732}_{-0.722}$, 2σ) for non-flat Λ CDM, XCDM, and ϕ CDM, respectively. C IV + Mg II data favour closed hypersurfaces in non-flat Λ CDM and non-flat XCDM, being $> 1\sigma$ (but $< 2\sigma$) and $\sim 1.1\sigma$

away from flat hypersurfaces, respectively, and favour open hypersurfaces in non-flat ϕ CDM, with flat hypersurfaces being within 1σ . C IV + Mg II data still provide weak constraints on w_X and α , but w_X constraints are more than 2σ away from $w_X = -1$ (Λ CDM).

C IV + Mg II data provide consistent (within 1σ) constraints on the intrinsic scatter, slope, and intercept parameters of both C IV and Mg II $R - L$ relations, which confirms that C IV and Mg II QSOs are standardizable through different $R - L$ relations.

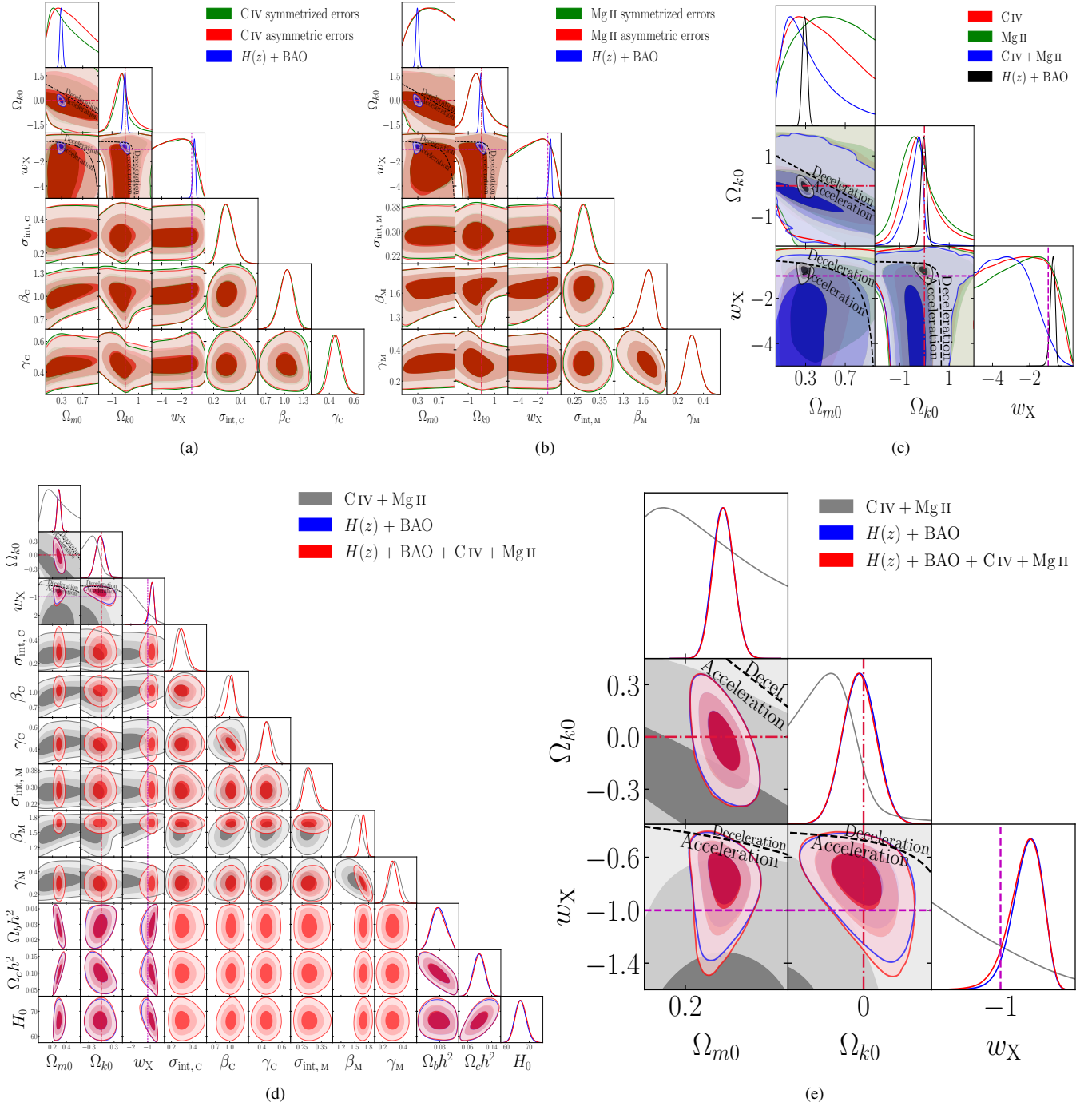


Figure 6. Same as Fig. 5 but for non-flat XCDM. The zero-acceleration black dashed lines are computed for the third cosmological parameter set to the $H(z)$ + BAO data best-fitting values listed in Table 2, and divide the parameter space into regions associated with currently-accelerating (either below left or below) and currently-decelerating (either above right or above) cosmological expansion. The crimson dash-dot lines represent flat hypersurfaces, with closed spatial hypersurfaces either below or to the left. The magenta dashed lines represent $w_X = -1$, i.e. non-flat Λ CDM.

5.2 Constraints from $H(z)$ + BAO + CIV + Mg II data

The mutually consistent cosmological-model parameter constraints allow us to jointly analyze $H(z)$ + BAO and CIV + Mg II data. In what follows we summarize the cosmological-model parameter constraints from $H(z)$ + BAO + CIV + Mg II data and contrast them with those from $H(z)$ + BAO data.

The $H(z)$ + BAO + CIV + Mg II data provide Ω_{m0} constraints

ranging from a low of 0.275 ± 0.023 (flat ϕ CDM) to a high of $0.301^{+0.015}_{-0.017}$ (flat Λ CDM), with a difference of 0.91σ , which only slightly differ from those determined using only $H(z)$ + BAO data.

The H_0 constraints from $H(z)$ + BAO + CIV + Mg II data range from a low of $65.68^{+2.20}_{-2.19}$ $\text{km s}^{-1} \text{Mpc}^{-1}$ (flat ϕ CDM) to a high of 69.15 ± 1.77 $\text{km s}^{-1} \text{Mpc}^{-1}$ (flat Λ CDM), with a difference of 1.23σ , which are 0.65σ (flat ϕ CDM) lower than and 0.35σ (flat

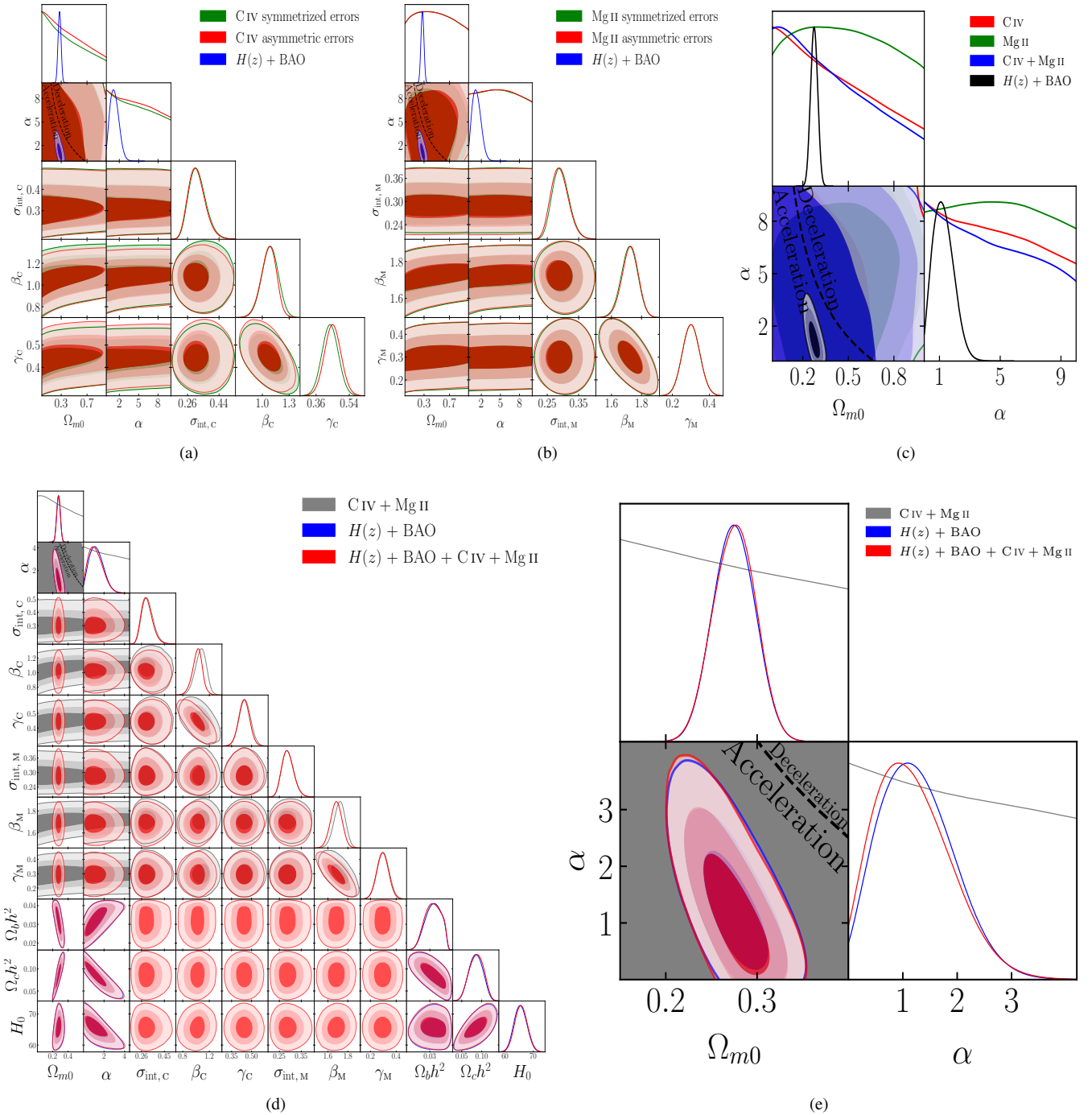


Figure 7. One-dimensional likelihood distributions and 1σ , 2σ , and 3σ two-dimensional likelihood confidence contours for flat ϕ CDM from various combinations of data. The zero-acceleration black dashed lines divide the parameter space into regions associated with currently-accelerating (below left) and currently-decelerating (above right) cosmological expansion. The $\alpha = 0$ axes correspond to flat Λ CDM.

Λ CDM higher than the median statistics estimate of $H_0 = 68 \pm 2.8$ $\text{km s}^{-1} \text{Mpc}^{-1}$ (Chen & Ratra 2011), and 2.94σ (flat ϕ CDM) and 1.84σ (flat Λ CDM) lower than the local Hubble constant measurement of $H_0 = 73.2 \pm 1.3$ $\text{km s}^{-1} \text{Mpc}^{-1}$ (Riess et al. 2021). The $H(z)$ + BAO + CIV + Mg II data provide H_0 constraints that are slightly higher ($\sim 0.1\sigma$ at most) and mostly more restrictive ($\sim 4\%$ at most) than those from $H(z)$ + BAO data.

The Ω_{k0} constraints from $H(z)$ + BAO + CIV + Mg II data are

$0.047^{+0.079}_{-0.089}$, -0.031 ± 0.108 , and $-0.044^{+0.090}_{-0.094}$ for non-flat Λ CDM, XCDM, and ϕ CDM, respectively, which are slightly lower ($\sim 0.1\sigma$ at most) than those from $H(z)$ + BAO data. Similar to the $H(z)$ + BAO data results, non-flat Λ CDM mildly favours open hypersurfaces, whereas non-flat XCDM and non-flat ϕ CDM mildly favour closed hypersurfaces. However, flat hypersurfaces are well within 1σ .

Dark energy dynamics is favoured. For flat (non-flat) XCDM, $w_X = -0.799^{+0.143}_{-0.111}$ ($w_X = -0.787^{+0.165}_{-0.102}$), with central values being

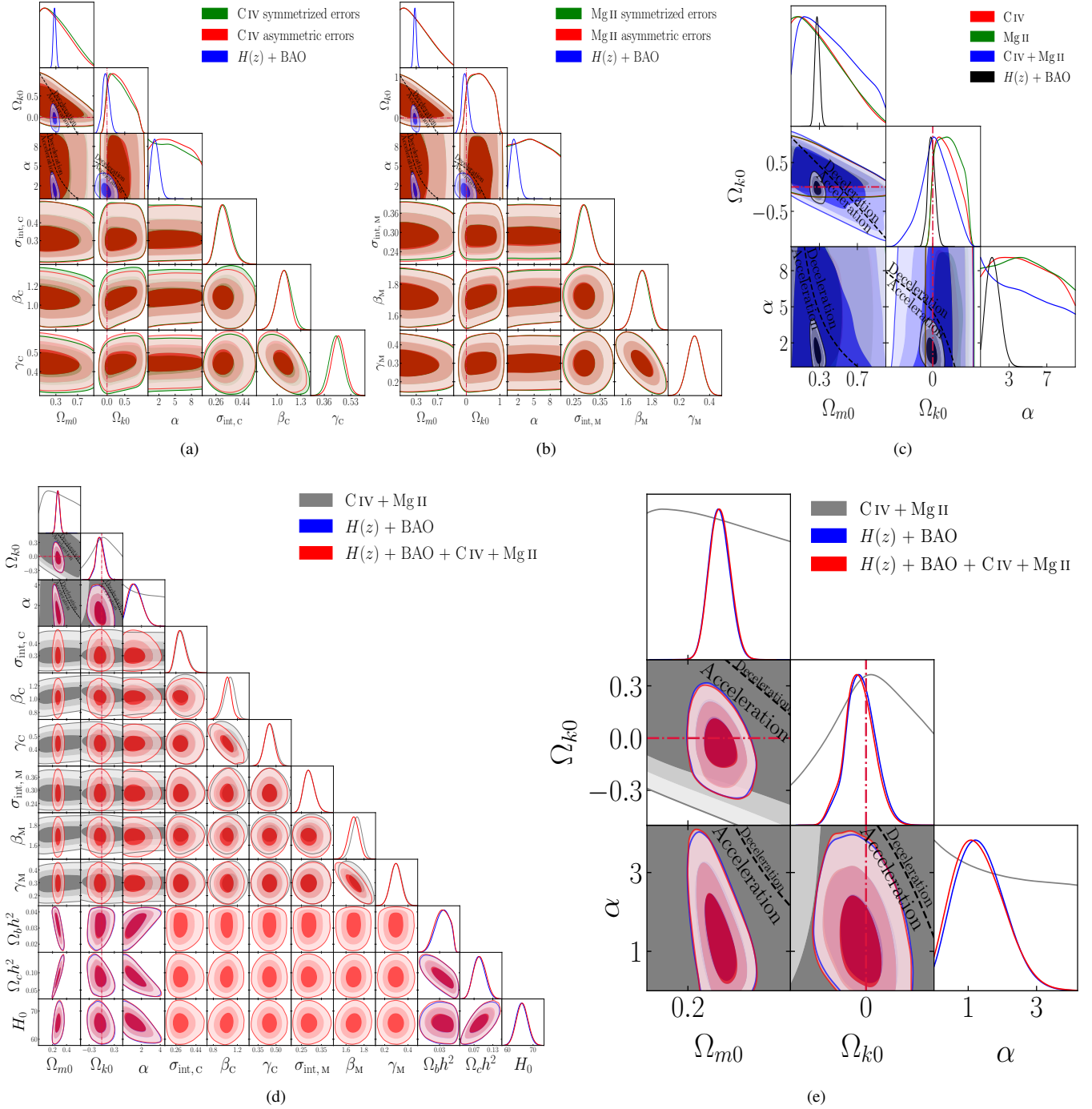


Figure 8. Same as Fig. 7 but for non-flat ϕ CDM. The zero-acceleration black dashed lines are computed for the third cosmological parameter set to the $H(z) + \text{BAO}$ data best-fitting values listed in Table 2, and divide the parameter space into regions associated with currently-accelerating (below left) and currently-decelerating (above right) cosmological expansion. The crimson dash-dot lines represent flat hypersurfaces, with closed spatial hypersurfaces either below or to the left. The $\alpha = 0$ axes correspond to non-flat Λ CDM.

1.81σ ($< 2\sigma$) higher than $w_X = -1$; and for flat (non-flat) ϕ CDM, $\alpha = 1.202^{+0.490}_{-0.862}$ ($\alpha = 1.320^{+0.572}_{-0.869}$), with central values being 1.39σ (1.52σ) away from $\alpha = 0$. The addition of C iv + Mg II data to $H(z) + \text{BAO}$ data bring w_X and α values lower, and closer to Λ CDM model values.

parameters are consistent with those from the individual data sets and the C iv + Mg II data.

As expected, the constraints on the C iv and Mg II $R - L$ relation

5.3 Model Comparison

From the AIC, BIC, and DIC values listed in Table 2, we find the following results (from the more correct C IV and Mg II asymmetric errors analyses):

1) **AIC.** $H(z) + \text{BAO}$ and $H(z) + \text{BAO} + \text{C IV} + \text{Mg II}$ data favour flat ϕCDM the most, and the evidence against the rest of the models/parametrizations is either only weak or positive.

C IV, Mg II, and C IV + Mg II data favour non-flat XCDM the most, however, in the C IV case, the evidence against non-flat ΛCDM and flat XCDM is only weak, the evidence against flat ΛCDM is positive, and the evidence against flat and non-flat ϕCDM is strong; in the Mg II case, the evidence against non-flat ΛCDM and flat XCDM is positive, the evidence against flat ΛCDM and flat ϕCDM is strong, and the evidence against non-flat ϕCDM is very strong; and in the C IV + Mg II case, the evidence against flat XCDM is positive, the evidence against non-flat ΛCDM is strong, and other models are very strongly disfavoured.

2) **BIC.** $H(z) + \text{BAO}$ and $H(z) + \text{BAO} + \text{C IV} + \text{Mg II}$ data favour flat ΛCDM the most, and in the former case, the evidence against the rest of the models/parametrizations is either only weak or positive, while in the latter case, the evidence against the rest of the models/parametrizations is either positive or strong (non-flat XCDM and non-flat ϕCDM).

C IV data favour non-flat ΛCDM the most, and the evidence against flat and non-flat XCDM is only weak, the evidence against flat ΛCDM is positive, and the evidence against flat and non-flat ϕCDM is strong.

Mg II and C IV + Mg II data favour non-flat XCDM the most, however, in the Mg II case, the evidence against non-flat ΛCDM , flat XCDM, and non-flat XCDM is only weak, the evidence against flat ϕCDM is strong, and the evidence against non-flat ϕCDM is very strong; and in the C IV + Mg II case, the evidence against non-flat ΛCDM and flat XCDM is positive, the evidence against flat ΛCDM is strong, and non-flat XCDM and non-flat ϕCDM are very strongly disfavoured.

3) **DIC.** $H(z) + \text{BAO}$ and $H(z) + \text{BAO} + \text{C IV} + \text{Mg II}$ data favour flat ϕCDM the most, and the evidence against the rest of the models/parametrizations is either only weak or positive.

C IV and Mg II data favour flat ΛCDM the most, however, in the former case, the evidence against the rest of the models/parametrizations is either only weak or positive, whereas in the latter case, the evidence against flat and non-flat ϕCDM is only weak, the evidence against non-flat ΛCDM and flat XCDM is positive, and the evidence against non-flat XCDM is strong.

C IV + Mg II data favour non-flat XCDM the most, and the evidence against the rest of the models/parametrizations is either only weak or positive.

Based on the more reliable DIC (Spiegelhalter et al. 2002; Liddle 2007), except for the Mg II data set, these data sets do not provide strong evidence against any of the cosmological models/parametrizations.

6 DISCUSSION

We have shown that QSOs with measured C IV time-delays can be standardized and so can be used as cosmological probes. Mg II QSOs are also standardizable and so can be jointly analyzed with C IV QSOs to constrain cosmological model parameters. This is not true for current H β QSOs (Khadka et al. 2022a) and more work is needed to clarify the H β QSO situation.

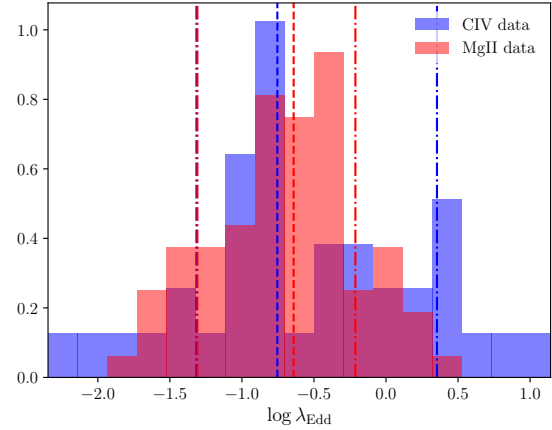


Figure 9. Normalized distributions of the Eddington ratio ($\log \lambda_{\text{Edd}}$) for the C IV sample (blue histogram) and for the Mg II sample (pink histogram). Vertical dashed lines stand for median values, while the dot-dashed lines represent 16- and 84-% percentiles. The bin size is $\Delta(\log \lambda_{\text{Edd}}) \sim 0.205$.

However, we find a 2.3σ difference in the measured slopes of the C IV and Mg II $R - L$ relations, in the flat ΛCDM model asymmetric error bars results of Table 3, or from the summary values of the measured C IV and Mg II $R - L$ relation slopes, $\gamma_{\text{C}} \approx 0.45 \pm 0.04$ and $\gamma_{\text{M}} \approx 0.3 \pm 0.05$. And while the C IV slope is only about 1σ lower than the $\gamma = 0.5$ slope predicted by simple photoionization theory (Bentz et al. 2013; Karas et al. 2021; Panda 2022) or a dust-based model of the BLR (Czerny & Hryniewicz 2011; Naddaf et al. 2021; Müller et al. 2022; Naddaf & Czerny 2022), the Mg II slope is about 4σ lower than $\gamma = 0.5$, which is more statistically significant.

In this section we examine potential (selection effect produced) differences between the C IV and Mg II compilations and conclude that the ones we study here are not very significant. We begin by computing the Eddington ratio λ_{Edd} for the 78 Mg II sources and the 38 C IV sources. We use the definition $\lambda_{\text{Edd}} = L_{\text{bol}}/L_{\text{Edd}}$ where the bolometric luminosity is estimated as a multiple of the corresponding monochromatic luminosity (L_{1350} for the C IV sample and L_{3000} for the Mg II sample; for the calculations in this section we adopt the fixed flat ΛCDM model with $\Omega_{m0} = 0.3$, $\Omega_{\Lambda} = 0.7$, and $H_0 = 70 \text{ km s}^{-1} \text{ Mpc}^{-1}$), taking into account the monochromatic luminosity-dependent bolometric correction factors according to Netzer (2019). Subsequently, we evaluate the correlations between λ_{Edd} and the monochromatic luminosity and the redshift.

The Eddington-ratio normalized distributions for the C IV and Mg II samples are shown in Fig. 9, represented by blue and pink histograms, respectively. The vertical dashed lines stand for the distribution medians, while vertical dot-dashed lines mark 16- and 84-% percentiles. For the Mg II sample, the λ_{Edd} distribution median is -0.64 , while 16- and 84-% percentiles are -1.31 and -0.21 , respectively. For the C IV sample, the median of the λ_{Edd} distribution is -0.75 , while 16- and 84-% percentiles are -1.32 and 0.35 , respectively. The median λ_{Edd} of the Mg II sources is larger than the median λ_{Edd} of the C IV sources. However, the C IV distribution is skewed significantly towards higher λ_{Edd} values, with a total range of $(-2.35, 1.14)$, in comparison with the range of $(-1.93, 0.50)$ for the Mg II sample. Also note that the Eddington ratios of the super-Eddington sources generally have large error bars, being consistent with the Eddington limit as well.

The $\lambda_{\text{Edd}}-z$ and $\lambda_{\text{Edd}}-L_{1350}$ or $\lambda_{\text{Edd}}-L_{3000}$ correlations are posi-

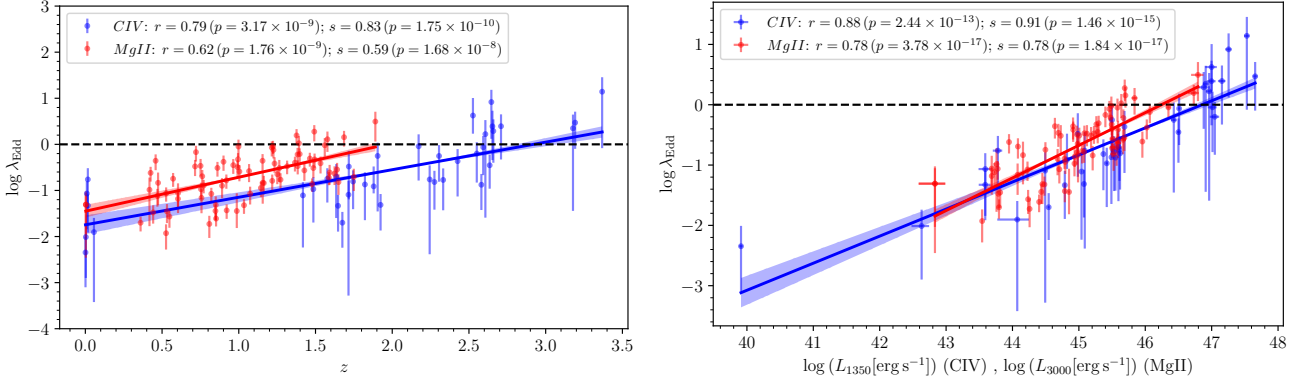


Figure 10. The Eddington ratio $\lambda_{\text{Edd}} = L_{\text{bol}}/L_{\text{Edd}}$ as a function of the source redshift (left panel) and as a function of the monochromatic luminosities L_{1350} or L_{3000} (right panel) for CIV (blue points) and Mg II (red points) sources. In both panels, we include the Pearson and the Spearman rank-order correlation coefficients (s), which indicate significant positive correlations between λ_{Edd} and z as well as λ_{Edd} and L_{1350} (or L_{3000}). The horizontal dashed line stands for the Eddington limit ($\log \lambda_{\text{Edd}} = 0$). The solid blue and red lines stand for the best-fitting linear relations for the CIV and Mg II datasets, respectively, see Eqs. (19) and Eqs. (20) for the best-fitting slopes and intercepts including 1σ uncertainties.

tive, see Fig. 10, left and right panels, respectively. The correlation significance is evaluated using Pearson and Spearman rank-order correlation coefficients, see the legend in Fig. 10. For both CIV and Mg II samples, the $\lambda_{\text{Edd}}-z$ correlation is positive and significant, being slightly stronger and more significant for CIV sources. The correlation between λ_{Edd} and the corresponding monochromatic luminosity is also positive and significant for both samples. Here we stress that the correlation between the Eddington ratio λ_{Edd} and the corresponding monochromatic luminosities is enhanced intrinsically due to the definition of $\lambda_{\text{Edd}} = L_{\text{bol}}/L_{\text{Edd}}$, where the bolometric luminosity is proportional to the monochromatic luminosity. However, the relative comparison of the correlation slopes provides hints about the similarities/differences of the two samples.

The slopes and the intercepts of the best-fitting linear relations between λ_{Edd} and z are

$$\begin{aligned} \log \lambda_{\text{Edd}}(\text{CIV}) &= (0.60 \pm 0.10)z - (1.75 \pm 0.20), \\ \log \lambda_{\text{Edd}}(\text{Mg II}) &= (0.74 \pm 0.12)z - (1.45 \pm 0.14), \end{aligned} \quad (19)$$

while for the best-fitting linear relations between λ_{Edd} and the monochromatic luminosity we obtain

$$\begin{aligned} \log \lambda_{\text{Edd}}(\text{CIV}) &= (0.45 \pm 0.04) \log L_{1350} - (21.03 \pm 1.97), \\ \log \lambda_{\text{Edd}}(\text{Mg II}) &= (0.54 \pm 0.05) \log L_{3000} - (25.01 \pm 2.25). \end{aligned} \quad (20)$$

The best-fitting relations are depicted in Fig. 10 including 1σ uncertainties of the best-fitting parameters. Compared to the CIV case, the Mg II Eddington ratios for the sample of 78 sources appear to increase more steeply with both redshift and monochromatic luminosity, though the Mg II and CIV slopes are consistent within 1.0σ (for the λ_{Edd} vs. z correlations) and 1.4σ (for the λ_{Edd} vs. monochromatic luminosity correlations), respectively. The differences in slopes may merely be due to the limited number of sources in each sample, and hence a selection effect.

However, when we study how the time-delay difference between the measured value and the value predicted from the best-fit $R-L$ relation (in the fixed flat Λ CDM model) — $\Delta\tau \equiv \log(\tau/\tau_{\text{RL}})$ (Martínez-Aldama et al. 2019; Zajaček et al. 2020a) — correlates with the Eddington ratio, the (anti)correlation is more significant and steeper for Mg II sources. This is shown in Fig. 11 for both CIV (blue points) and Mg II sources (red points). As a caveat, we note that unless the SMBH mass is inferred independently of the RM, $\Delta\tau$ and $\log \lambda_{\text{Edd}}$ are intrinsically correlated as $\Delta\tau \propto -\log \tau$, which

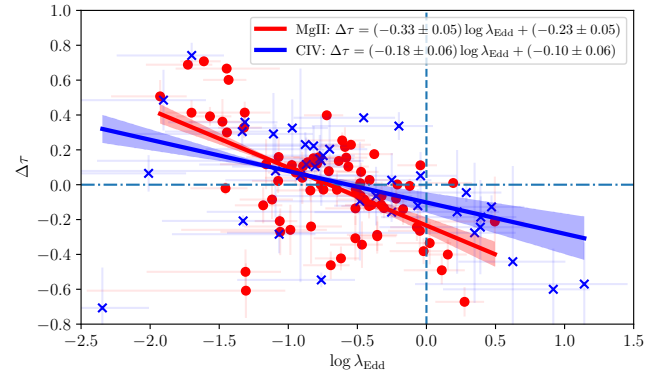


Figure 11. (Anti)correlation between $\Delta\tau \equiv \log(\tau/\tau_{\text{RL}})$ and the Eddington ratio λ_{Edd} for both CIV sources (blue points) and Mg II sources (red points). The correlation is more significant for the Mg II sample with a Spearman rank-order correlation coefficient of -0.53 ($p = 4.76 \times 10^{-7}$) in comparison with -0.50 ($p = 0.0015$) for the CIV sample. The slope of the anticorrelation is steeper for Mg II sources, see Eq. (21) for the comparison.

implies anticorrelation.⁹ Therefore, we can only assess the different behaviour between $\Delta\tau$ and λ_{Edd} based on the relative comparison of the correlation coefficients and the correlation slopes for the two samples. The anticorrelation between $\Delta\tau$ and $\log \lambda_{\text{Edd}}$ is more significant for the Mg II sample with a Spearman rank-order correlation coefficient of $s = -0.53$ ($p = 4.76 \times 10^{-7}$), while for the CIV sample we obtain $s = -0.50$ ($p = 0.0015$). When we fit a linear function to the anticorrelations we get

$$\begin{aligned} \Delta\tau(\text{CIV}) &= (-0.18 \pm 0.06) \log \lambda_{\text{Edd}} + (-0.10 \pm 0.06), \\ \Delta\tau(\text{Mg II}) &= (-0.33 \pm 0.05) \log \lambda_{\text{Edd}} + (-0.23 \pm 0.05). \end{aligned} \quad (21)$$

⁹ It is generally thought advisable to use independent accretion-rate proxies, such as the relative Fe II strength $\mathcal{R}_{\text{Fe II}}$ the variability factor F_{var} (Martínez-Aldama et al. 2020b), or the shape of the ionizing continuum (Panda et al. 2019b; Fonseca Alvarez et al. 2020; Ferland et al. 2020), rather than the Eddington ratio, due to the interdependency on the rest-frame time delay and the monochromatic luminosity that appear in the $R-L$ correlation. However, here we focus on a relative comparison between the Mg II and CIV samples instead of the absolute values of the correlation slopes and normalizations.

Hence, the anticorrelation is significantly steeper for the Mg II sample (by nearly a factor of two) in comparison with the current C IV sample. A combination of steeper $\Delta\tau - \log \lambda_{\text{Edd}}$ anticorrelation with a slightly steeper correlation between $\log \lambda_{\text{Edd}}$ and the monochromatic luminosity for the Mg II sources can qualitatively account for the flatter Mg II $R - L$ relation with respect to the C IV one. However, with a future increase in the number of Mg II and C IV RM sources, both towards lower and higher redshifts, the difference in the correlation slopes is expected to become progressively weaker, since the general trends appear to be consistent between the Mg II and the C IV samples and the differences can be traced to a few outlying sources.

There may also be a potential problem in the way λ_{Edd} was measured in the C IV QSOs. Such measurements are uncertain, particularly for C IV. The C IV-emitting material is likely not completely virialized as revealed by its blueshift and blueward asymmetry with respect to low-ionization lines, which hints at an outflow approaching the observer. Therefore, the SMBH mass determination may be biased (Baskin & Laor 2005). The anticorrelation between the virial factor and the C IV FWHM is also the most uncertain among broad lines due to the smallest correlation coefficient as investigated by Mejía-Restrepo et al. (2018), which results in larger errorbars of C IV Eddington ratios in comparison with Mg II ones in Fig. 10. Looking at how the C IV sample was selected might suggest that the histogram in Fig. 9 may not well represent the true C IV λ_{Edd} values. One of the criteria used when selecting the final C IV QSOs from the SDSS-RM sample is the variability of the light curve. Sources with no significant variability were excluded from the final sample to ensure a reliable time-lag estimate (Grier et al. 2019). Several papers claim that there is a negative correlation between the variability and the Eddington ratio (e.g. De Cicco et al. 2022, and references therein). This suggests that the criterion of the variability applied to the SDSS-RM sample excludes highly-radiating QSOs. Such QSOs flatten the $R - L$ relation and increase the scatter in the case of the H β $R - L$ relation, which is not observed in the C IV $R - L$ relation. In addition, Kaspi et al. (2021) claim that their three sources do not show strong outflows, which are usually found in QSOs with high Eddington ratios (Coatman et al. 2017; Martínez-Aldama et al. 2018). We performed a visual inspection of the rest of the sources and most of them show spectral features associated with low Eddington ratios (symmetric profiles in C IV $\lambda 1549$, moderate He II $\lambda 1640$ contribution, strong contribution of C III] $\lambda 1909$, and low contributions of Fe II and Fe III). All these facts, in contradiction to Fig. 9, suggest that the C IV sample mainly includes low Eddington sources. However, a detailed analysis of variability and spectral properties is needed to confirm the accretion state of sources in the C IV sample.

The C IV sample spans eight orders of luminosity ($L_{1350} \sim 10^{40-48} \text{ erg s}^{-1}$) and covers a large redshift range ($0.001 < z < 3.37$), and is standardizable and suitable for constraining cosmological models. The Mg II sample has smaller luminosity and redshift ranges ($L_{3000} \sim 10^{43-47} \text{ erg s}^{-1}$, $0 < z < 1.8$), but is standardizable and also suitable for constraining cosmological parameters (Khadka et al. 2021a; Khadka et al. 2022b), and can be jointly analyzed with the C IV sample. The same is not true for the H β sample. Although the H β sample spans almost five orders of luminosity ($L_{5100} = 10^{41.5-46} \text{ erg s}^{-1}$), the redshift range is narrow ($0.002 < z < 0.9$), but most importantly the current H β sample appears to be not standardizable (Khadka et al. 2022a). Therefore, we cannot jointly use the Mg II, C IV and H β samples, which is unfortunate since they together contain more sources over large luminosity and redshift ranges, all of which are beneficial if such QSOs are to be useful for cosmological purposes.

With future missions and surveys, such as the Black Hole Map-

per by the SDSS-V (Kollmeier et al. 2017), long-term spectroscopic and photometric measurements of reverberation lags for the continuum and the “major” emission lines (C IV, Mg II, and H β /H α) will be obtained for a large sample of quasars, adding wide-area, multi-epoch optical spectroscopy to the era of time-domain imaging. With the photometric Legacy Survey of Space and Time performed by the Vera C. Rubin observatory (Ivezić et al. 2019), many more RM objects will be obtained, e.g. the Rubin Deep Drilling Field should result in a few thousand measurements at redshifts $\sim 1 - 2$ (Kovačević et al. 2022; Brandt et al. 2018). This will lead to the decrease in the statistical error. The source monitoring will be performed photometrically in six broad optical bands, which will be used to probe the continuum accretion-disc response as well as the BLR response using the photometric RM (see e.g., Panda et al. 2019a; Martínez Aldama et al. 2020a, for the assessment of the photometric RM for BLR RM and the future application in cosmology). Currently, we obtain a difference with respect to BAO+ $H(z)$ data constraints by at most 0.1σ when 116 C IV + Mg II sources are included, hence a QSO dataset larger by an order of magnitude can naturally influence the overall cosmological constraints more. It is more challenging to lower the dispersion in the individual time-delay measurements. Using a consistent methodology for all the RM QSOs to infer time-delays will be necessary to avoid systematic errors introduced by combining different subsets of RM sources into one large dataset. Specifically, surveys and RM projects typically select sources in a narrow luminosity range, which can result in a problem. For instance, if the time-delay method used for higher-luminosity sources is systematically susceptible to yield smaller lags in comparison with the method used for lower-luminosity sources, it can lead to a systematically smaller slope of the R-L relation compared to the case when the same method is applied to all the sources across several orders of magnitude in luminosity.

7 CONCLUSIONS

In this paper, for the first time, we use 38 highest-quality C IV QSO data to simultaneously constrain cosmological model parameters, in six cosmological models, and C IV $R - L$ relation parameters. We use a new technique we have developed to more correctly take into account the asymmetric time-lag τ error bars and applied it to both C IV and Mg II QSO data (Khadka et al. 2021a) for the first time. We find that similar to Mg II QSO data, C IV QSO data are also standardizable through the $R - L$ relation since the C IV $R - L$ relation parameters are cosmological model-independent. Unlike the H β QSOs cosmological constraints (Khadka et al. 2022a), those from C IV and Mg II QSO data are consistent with cosmological constraints from better established $H(z) + \text{BAO}$ data.

The mutually consistent cosmological parameter constraints from C IV, Mg II, and $H(z) + \text{BAO}$ data allow us to perform joint analyses on C IV + Mg II data as well as on $H(z) + \text{BAO} + \text{C IV} + \text{Mg II}$ data. Although the joint C IV + Mg II cosmological constraints are still weak, they do slightly ($\sim 0.1\sigma$ at most) alter the $H(z) + \text{BAO}$ constraints when jointly analyzed.

The Rubin Observatory Legacy Survey of Space and Time (Ivezić et al. 2019), as well as the SDSS-V Black Hole Mapper (Kollmeier et al. 2017), will find many more C IV and Mg II QSOs. These new QSOs will result in significantly more restrictive C IV (and Mg II) cosmological constraints than the first ones we have derived here.

Table 2: Unmarginalized best-fitting parameter values for all models from various combinations of data.

Model	Data set	$\Omega_b h^2$	$\Omega_c h^2$	Ω_{m0}	Ω_{k0}	w_X/α^a	H_0^b	$\sigma_{\text{int},c}$	γ_c	β_c	$\sigma_{\text{int},M}$	γ_M	β_M	$-2\ln\mathcal{L}_{\text{max}}$	AIC	BIC	DIC	ΔAIC	ΔBIC	ΔDIC	
Flat Λ CDM	$H(z) + \text{BAO}$	0.0244	0.1181	0.301	-	-	68.98	-	-	-	-	-	-	25.64	31.64	36.99	32.32	0.00	0.00	0.00	
	Mg II QSO syymm	-	0.0518	0.157	-	-	-	-	-	-	0.282	0.285	1.670	30.16	38.16	47.59	37.68	0.00	0.00	0.00	
	Mg II QSO asymm	-	0.0472	0.148	-	-	-	-	-	-	0.278	0.282	1.676	30.18	38.18	47.61	37.86	0.00	0.00	0.00	
	C IV QSO syymm	-	-0.0007	0.050	-	-	-	-	0.275	0.403	0.989	-	-	20.61	28.61	35.16	31.10	0.00	0.00	0.00	
	C IV QSO asymm	-	-0.0026	0.046	-	-	-	-	0.265	0.411	0.980	-	-	20.51	28.51	35.06	32.74	0.00	0.00	0.00	
Non-flat Λ CDM	C IV QSO asymm + Mg II QSO asymm	-	0.0082	0.068	-	-	-	0.274	0.412	0.995	0.280	0.286	1.647	50.94	64.94	84.94	69.10	0.00	0.00	0.00	
	$H(z) + \text{BAO} + \text{C IV QSO asymm} + \text{Mg II QSO asymm}$	0.0245	0.1148	0.295	-	-	68.86	0.284	0.421	1.079	0.279	0.288	1.688	78.31	96.31	123.98	98.13	0.00	0.00	0.00	
	$H(z) + \text{BAO}$	0.0260	0.1098	0.292	0.048	-	-	68.55	-	-	-	-	-	25.30	33.30	40.43	33.87	1.66	3.44	1.54	
	Mg II QSO syymm	-	0.1703	0.399	-1.135	-	-	-	-	-	0.275	0.352	1.625	25.39	35.39	47.17	40.12	-2.77	-0.42	2.44	
	Mg II QSO asymm	-	0.1708	0.400	-1.134	-	-	-	-	-	0.270	0.349	1.635	25.62	35.62	47.40	40.25	-2.56	-0.20	2.38	
Flat XCDM	C IV QSO syymm	-	0.0147	0.081	-0.358	-	-	0.237	0.486	0.968	-	-	-	9.38	19.38	27.57	36.94	-9.23	-7.59	5.84	
	C IV QSO asymm	-	0.0378	0.128	-0.471	-	-	0.242	0.498	0.939	-	-	-	14.44	24.44	32.63	36.77	-4.07	-2.43	4.03	
	C IV QSO asymm + Mg II QSO asymm	-	0.0791	0.213	-0.678	-	-	0.269	0.512	1.018	0.279	0.293	1.642	42.92	58.92	80.95	68.83	-6.01	-3.26	-0.27	
	$H(z) + \text{BAO} + \text{C IV QSO asymm} + \text{Mg II QSO asymm}$	0.0260	0.1112	0.293	0.036	-	-	68.64	0.278	0.430	1.045	0.278	0.293	1.684	78.09	98.09	128.84	99.73	1.79	4.86	1.60
	$H(z) + \text{BAO}$	0.0296	0.0951	0.290	-	-	-0.754	65.79	-	-	-	-	-	22.39	30.39	37.52	30.63	-1.25	0.53	-1.69	
Non-flat XCDM	Mg II QSO syymm	-	-0.0234	0.003	-	-	-4.949	-	-	0.270	0.241	1.354	24.39	34.39	46.18	41.19	-3.77	-1.41	3.51		
	Mg II QSO asymm	-	-0.0226	0.005	-	-	-4.983	-	-	0.267	0.249	1.361	24.35	34.35	46.13	41.14	-3.83	-1.48	3.28		
	C IV QSO syymm	-	-0.0237	0.003	-	-	-4.990	-	0.234	0.321	0.727	-	-	12.69	22.69	30.88	31.64	-5.92	-4.29	0.53	
	C IV QSO asymm	-	-0.0203	0.010	-	-	-4.988	-	0.232	0.355	0.736	-	-	15.58	25.58	33.77	33.67	-2.93	-1.29	0.93	
	C IV QSO asymm + Mg II QSO asymm	-	-0.0212	0.008	-	-	-4.875	-	0.225	0.337	0.757	0.262	0.248	1.399	40.24	56.24	78.27	66.94	-8.70	-5.95	-2.16
Non-flat XCDM	$H(z) + \text{BAO} + \text{C IV QSO asymm} + \text{Mg II QSO asymm}$	0.0283	0.1007	0.297	-	-	-0.792	0.283	0.425	1.074	0.279	0.286	1.691	75.85	95.85	126.60	97.19	-0.46	2.62	-0.94	
	$H(z) + \text{BAO}$	0.0289	0.0985	0.296	-0.053	-	-0.730	65.76	-	-	-	-	-	22.13	32.13	41.05	32.51	0.49	4.06	0.19	
	Mg II QSO syymm	-	-0.0103	0.030	-0.060	-	-3.207	-	-	0.257	0.284	1.382	1.829	18.29	30.29	44.43	46.23	-7.87	-3.16	8.54	
	Mg II QSO asymm	-	-0.0016	0.048	-0.095	-	-2.947	-	-	0.260	0.303	1.395	1.966	19.66	31.66	45.80	45.06	-6.52	-1.81	7.19	
	C IV QSO syymm	-	-0.0161	0.019	-0.035	-	-3.815	-	0.220	0.428	0.827	-	-	6.26	18.26	28.09	38.74	-10.35	-7.08	7.64	
Flat ϕ CDM	C IV QSO asymm	-	-0.0130	0.025	-0.042	-	-4.329	-	0.228	0.386	0.828	-	-	12.08	24.08	33.90	37.86	-4.43	-1.16	5.12	
	C IV QSO asymm + Mg II QSO asymm	-	-0.0149	0.021	-0.034	-	-5.000	-	0.226	0.374	0.808	0.270	0.285	1.262	32.43	50.43	75.21	68.46	-14.51	-9.00	-0.71
	$H(z) + \text{BAO} + \text{C IV QSO asymm} + \text{Mg II QSO asymm}$	0.0281	0.1046	0.296	-0.065	-	-0.779	67.10	0.276	0.434	1.064	0.274	0.298	1.676	75.81	97.81	131.64	98.92	1.51	7.66	0.79
	$H(z) + \text{BAO}$	0.0310	0.0900	0.280	-	-	1.010	65.89	-	-	-	-	-	22.31	30.31	37.45	29.90	-1.33	0.46	-2.42	
	Mg II QSO syymm	-	0.0414	0.136	-	-	0.018	-	-	0.282	0.282	1.668	1.668	30.17	40.17	51.96	38.18	2.01	4.37	0.50	
Non-flat ϕ CDM	Mg II QSO asymm	-	0.0532	0.160	-	-	0.047	-	-	0.279	0.284	1.679	2.020	30.20	40.20	51.99	38.40	2.02	4.38	0.52	
	C IV QSO syymm	-	0.0003	0.052	-	-	0.030	-	0.274	0.399	0.996	-	-	20.67	30.67	38.85	33.47	2.05	3.69	2.37	
	C IV QSO asymm	-	-0.0059	0.039	-	-	0.061	-	0.270	0.410	0.977	-	-	20.59	30.59	38.78	34.56	2.08	3.72	1.82	
	C IV QSO asymm + Mg II QSO asymm	-	-0.0078	0.035	-	-	0.014	-	0.263	0.399	0.984	0.283	0.265	1.662	51.19	67.19	89.21	72.04	2.25	5.00	2.94
	$H(z) + \text{BAO} + \text{C IV QSO asymm} + \text{Mg II QSO asymm}$	0.0289	0.0985	0.288	-	-	0.663	66.68	0.275	0.430	1.050	0.278	0.304	1.668	75.78	95.78	126.54	96.48	-0.52	2.55	-1.65
Non-flat ϕ CDM	$H(z) + \text{BAO}$	0.0306	0.0920	0.284	-0.058	-	1.200	65.91	-	-	-	-	-	22.05	32.05	40.97	31.30	0.41	3.98	-1.02	
	Mg II QSO syymm	-	0.1167	0.290	-0.277	-	0.000	-	-	0.283	0.290	1.678	1.678	29.81	41.81	55.95	38.70	3.65	8.36	1.02	
	Mg II QSO asymm	-	0.1354	0.328	-0.310	-	0.042	-	-	0.275	0.292	1.675	1.675	29.91	41.91	56.05	38.65	3.73	8.45	0.78	
	C IV QSO syymm	-	0.0489	0.151	-0.146	-	0.065	-	0.272	0.417	1.010	-	-	20.42	32.42	42.24	34.07	3.80	7.08	2.96	
	C IV QSO asymm	-	0.0367	0.126	-0.125	-	0.121	-	0.268	0.423	1.006	-	-	20.41	32.41	42.24	34.92	3.91	7.18	2.18	
Non-flat ϕ CDM	C IV QSO asymm + Mg II QSO asymm	-	0.0611	0.176	-0.173	-	0.115	-	0.264	0.421	1.034	0.271	0.289	50.74	68.74	93.52	72.86	3.80	9.31	3.76	
	$H(z) + \text{BAO} + \text{C IV QSO asymm} + \text{Mg II QSO asymm}$	0.0313	0.0882	0.278	-0.044	-	1.256	65.76	0.281	0.455	1.035	0.276	0.292	1.687	97.73	131.55	97.61	1.42	7.57	-0.52	

^a w_X corresponds to flat/non-flat XCDM and α corresponds to flat/non-flat ϕ CDM.

^b $\text{km s}^{-1} \text{Mpc}^{-1}$. Ω_b and H_0 are set to be 0.05 and $70 \text{ km s}^{-1} \text{Mpc}^{-1}$, respectively.

Table 3: One-dimensional marginalized posterior mean values and uncertainties ($\pm 1\sigma$ error bars or 2σ limits) of the parameters for all models from various combinations of data.

Model	Data set	$\Omega_b h^2$	$\Omega_c h^2$	Ω_{M0}	Ω_{M0}	H_0	$\sigma_{\text{int},c}$	γ_c	β_c	$\sigma_{\text{int},M}$	γ_M	β_M
Flat Λ CDM	$H(z) + \text{BAO}$	0.0247 ± 0.0030	$0.1186^{+0.0076}_{-0.0083}$	$0.301^{+0.016}_{-0.018}$	$0.470^{+0.016}_{-0.016}$	69.14 ± 1.85	-	-	-	$0.293^{+0.023}_{-0.023}$	0.297 ± 0.047	$1.698^{+0.063}_{-0.064}$
	Mg II QSO symm	-	-	-	-	-	-	-	-	$0.290^{+0.024}_{-0.030}$	0.296 ± 0.047	$1.703^{+0.064}_{-0.057}$
	Mg II QSO asymm	-	-	-	-	-	-	-	-	-	-	-
	C IV QSO asymm	-	-	$< 0.471^\circ$	-	-	-	$0.311^{+0.039}_{-0.036}$	0.427 ± 0.043	1.051 ± 0.096	-	-
Non-flat ϕ CDM	C IV QSO asymm	-	-	$< 0.503^\circ$	-	-	$0.307^{+0.039}_{-0.039}$	0.441 ± 0.044	$1.034^{+0.097}_{-0.087}$	-	-	-
	C IV QSO asymm + Mg II QSO asymm	-	-	$< 0.444^\circ$	-	-	$0.305^{+0.039}_{-0.039}$	0.440 ± 0.042	1.030 ± 0.089	$0.289^{+0.023}_{-0.023}$	0.292 ± 0.045	1.691 ± 0.061
	C IV QSO asymm + Mg II QSO asymm	0.0247 ± 0.0028	$0.1183^{+0.0073}_{-0.0080}$	$0.301^{+0.015}_{-0.017}$	-	69.15 ± 1.77	-	$0.303^{+0.036}_{-0.036}$	0.442 ± 0.039	$0.288^{+0.023}_{-0.029}$	0.294 ± 0.044	1.686 ± 0.056
	C IV QSO asymm + Mg II QSO asymm	$0.0266^{+0.0039}_{-0.0045}$	0.1088 ± 0.0166	0.291 ± 0.023	-	68.37 ± 2.10	-	-	-	$0.291^{+0.024}_{-0.030}$	$0.315^{+0.049}_{-0.056}$	1.687 ± 0.067
Non-flat Λ CDM	Mg II QSO symm	-	-	$0.568^{+0.359}_{-0.196}$	$-0.427^{+0.546}_{-0.453}$	-	-	-	-	$0.288^{+0.024}_{-0.031}$	$0.316^{+0.070}_{-0.057}$	$1.693^{+0.070}_{-0.064}$
	Mg II QSO asymm	-	-	$0.567^{+0.368}_{-0.192}$	$-0.419^{+0.560}_{-0.449}$	-	-	-	-	-	-	-
	C IV QSO symm	-	-	$0.417^{+0.133}_{-0.133}$	$-0.478^{+0.346}_{-0.351}$	-	-	$0.300^{+0.041}_{-0.036}$	$0.465^{+0.047}_{-0.042}$	1.072 ± 0.098	-	-
	C IV QSO asymm	-	-	$0.467^{+0.168}_{-0.168}$	$-0.330^{+0.391}_{-0.391}$	-	-	$0.305^{+0.036}_{-0.036}$	$0.468^{+0.097}_{-0.086}$	$1.059^{+0.097}_{-0.086}$	-	-
Non-flat ϕ CDM	C IV QSO asymm + Mg II QSO asymm	-	-	$0.473^{+0.178}_{-0.178}$	$-0.818^{+0.391}_{-0.391}$	-	-	$0.299^{+0.036}_{-0.036}$	$0.491^{+0.050}_{-0.050}$	$0.285^{+0.023}_{-0.023}$	$0.314^{+0.048}_{-0.052}$	1.662 ± 0.065
	C IV QSO asymm + Mg II QSO asymm	$0.0262^{+0.0037}_{-0.0044}$	0.1105 ± 0.0165	0.292 ± 0.022	-	68.55 ± 2.05	-	$0.303^{+0.036}_{-0.036}$	0.441 ± 0.039	$0.288^{+0.023}_{-0.030}$	0.294 ± 0.043	1.685 ± 0.055
	C IV QSO asymm + Mg II QSO asymm	$0.0295^{+0.0042}_{-0.0050}$	$0.0969^{+0.0178}_{-0.0152}$	0.289 ± 0.020	-	$66.22^{+2.31}_{-2.54}$	-	-	-	$0.291^{+0.024}_{-0.030}$	0.294 ± 0.048	$1.640^{+0.118}_{-0.118}$
	C IV QSO asymm + Mg II QSO asymm	$0.0292^{+0.0040}_{-0.0050}$	$0.0983^{+0.0181}_{-0.0144}$	$0.290^{+0.020}_{-0.018}$	-	$66.45^{+2.28}_{-2.53}$	-	$0.292^{+0.041}_{-0.036}$	0.403 ± 0.047	0.957 ± 0.128	$0.288^{+0.023}_{-0.030}$	0.295 ± 0.047
Non-flat ϕ CDM	C IV QSO asymm + Mg II QSO asymm	$0.0294^{+0.0047}_{-0.0050}$	$0.0980^{+0.0186}_{-0.0187}$	0.292 ± 0.025	-	$66.13^{+2.35}_{-2.36}$	-	$0.296^{+0.041}_{-0.036}$	0.426 ± 0.049	$0.970^{+0.136}_{-0.136}$	$0.283^{+0.023}_{-0.023}$	$0.282^{+0.042}_{-0.046}$
	C IV QSO asymm + Mg II QSO asymm	$0.0290^{+0.0044}_{-0.0053}$	$0.0997^{+0.0186}_{-0.0188}$	0.293 ± 0.025	-	$66.41^{+2.26}_{-2.49}$	-	$0.282^{+0.036}_{-0.036}$	0.405 ± 0.047	$0.900^{+0.122}_{-0.122}$	$0.285^{+0.023}_{-0.023}$	$0.282^{+0.042}_{-0.046}$
	C IV QSO asymm + Mg II QSO asymm	$0.0290^{+0.0044}_{-0.0053}$	$0.0997^{+0.0186}_{-0.0188}$	0.293 ± 0.025	-	$66.41^{+2.26}_{-2.49}$	-	$0.305^{+0.036}_{-0.036}$	0.443 ± 0.039	$1.021^{+0.122}_{-0.122}$	$0.289^{+0.023}_{-0.030}$	0.295 ± 0.044
	C IV QSO asymm + Mg II QSO asymm	$0.0294^{+0.0047}_{-0.0050}$	$0.0980^{+0.0186}_{-0.0187}$	0.292 ± 0.025	-	$66.13^{+2.35}_{-2.36}$	-	$0.297^{+0.042}_{-0.036}$	0.443 ± 0.045	$1.028^{+0.121}_{-0.121}$	$0.280^{+0.023}_{-0.030}$	$0.319^{+0.048}_{-0.054}$
Flat ϕ CDM	C IV QSO asymm + Mg II QSO asymm	$0.0318^{+0.0053}_{-0.0045}$	$0.0866^{+0.0190}_{-0.0171}$	0.275 ± 0.023	-	$65.68^{+2.20}_{-2.19}$	-	$0.302^{+0.036}_{-0.036}$	$0.453^{+0.051}_{-0.051}$	$1.025^{+0.119}_{-0.119}$	$0.289^{+0.023}_{-0.030}$	$1.526^{+0.132}_{-0.108}$
	C IV QSO asymm + Mg II QSO asymm	$0.0320^{+0.0054}_{-0.0041}$	$0.0855^{+0.0175}_{-0.0174}$	0.275 ± 0.023	-	$65.47^{+2.22}_{-2.21}$	-	$0.318^{+0.039}_{-0.039}$	0.456 ± 0.043	1.086 ± 0.090	$0.294^{+0.023}_{-0.029}$	1.719 ± 0.054
	C IV QSO asymm + Mg II QSO asymm	$0.0320^{+0.0054}_{-0.0041}$	$0.0855^{+0.0175}_{-0.0174}$	0.275 ± 0.023	-	$65.47^{+2.22}_{-2.21}$	-	$0.314^{+0.038}_{-0.038}$	0.450 ± 0.044	$1.070^{+0.092}_{-0.075}$	$0.290^{+0.024}_{-0.030}$	$1.724^{+0.055}_{-0.051}$
	C IV QSO asymm + Mg II QSO asymm	$0.0318^{+0.0053}_{-0.0045}$	$0.0866^{+0.0190}_{-0.0171}$	0.275 ± 0.023	-	$65.68^{+2.20}_{-2.19}$	-	$0.312^{+0.037}_{-0.037}$	0.449 ± 0.043	$1.069^{+0.091}_{-0.074}$	$0.289^{+0.023}_{-0.030}$	$1.717^{+0.059}_{-0.053}$
Non-flat ϕ CDM	C IV QSO asymm + Mg II QSO asymm	$0.0320^{+0.0057}_{-0.0058}$	$0.0865^{+0.0172}_{-0.0198}$	$0.277^{+0.023}_{-0.026}$	-	65.53 ± 2.19	-	$0.306^{+0.036}_{-0.036}$	0.444 ± 0.040	$1.019^{+0.119}_{-0.119}$	0.295 ± 0.044	1.683 ± 0.056
	C IV QSO asymm + Mg II QSO asymm	$0.0320^{+0.0057}_{-0.0058}$	$0.0865^{+0.0172}_{-0.0198}$	$0.277^{+0.023}_{-0.026}$	-	65.53 ± 2.19	-	$0.319^{+0.039}_{-0.039}$	0.437 ± 0.043	1.089 ± 0.089	0.300 ± 0.046	1.721 ± 0.054
	C IV QSO asymm + Mg II QSO asymm	$0.0320^{+0.0057}_{-0.0058}$	$0.0865^{+0.0172}_{-0.0198}$	$0.277^{+0.023}_{-0.026}$	-	65.53 ± 2.19	-	$0.313^{+0.039}_{-0.039}$	0.451 ± 0.043	$1.076^{+0.087}_{-0.087}$	0.301 ± 0.047	1.724 ± 0.056
	C IV QSO asymm + Mg II QSO asymm	$0.0317^{+0.0058}_{-0.0043}$	$0.0884^{+0.0183}_{-0.0203}$	$0.278^{+0.026}_{-0.026}$	-	65.77 ± 2.21	-	$0.312^{+0.037}_{-0.037}$	0.450 ± 0.043	$1.072^{+0.076}_{-0.076}$	$0.299^{+0.023}_{-0.030}$	1.719 ± 0.055

^a w_X corresponds to flat/non-flat Λ CDM and α corresponds to flat/non-flat ϕ CDM.^b km s^{-1} , Ω_b and H_0 are set to be 0.05 and $70 \text{ km s}^{-1} \text{ Mpc}^{-1}$, respectively.^c This is the 1σ limit. The 2σ limit is set by the prior and not shown here.

ACKNOWLEDGEMENTS

This research was supported in part by US DOE grant DE-SC0011840, by the Polish Funding Agency National Science Centre, project 2017/26/A/ST9/00756 (Maestro 9), by GAČR EXPRO grant 21-13491X, by Millenium Nucleus NCN19_058 (TITANs), and by the Conselho Nacional de Desenvolvimento Científico e Tecnológico (CNPq) Fellowship (164753/2020-6). The authors acknowledge the Czech-Polish mobility program (MŠMT 8J20PL037 and PPN/BCZ/2019/1/00069). Part of the computation for this project was performed on the Beocat Research Cluster at Kansas State University.

DATA AVAILABILITY

The data analysed in this article are listed in Table A1 of this paper and in table A1 of Khadka et al. (2021a).

REFERENCES

- Abdalla E., et al., 2022, *J. High En. Astrophys.*, 34, 49
- Arjona R., Nesseris S., 2021, *Phys. Rev. D*, 103, 103539
- Audren B., Lesgourgues J., Benabed K., Prunet S., 2013, *J. Cosmology Astropart. Phys.*, 2013, 001
- Baskin A., Laor A., 2005, *MNRAS*, 356, 1029
- Bentz M. C., et al., 2013, *ApJ*, 767, 149
- Blas D., Lesgourgues J., Tram T., 2011, *J. Cosmology Astropart. Phys.*, 2011, 034
- Brandt W. N., et al., 2018, preprint, (arXiv:1811.06542)
- Brinckmann T., Lesgourgues J., 2019, *Physics of the Dark Universe*, 24, 100260
- Britzen S., et al., 2021, *MNRAS*, 503, 3145
- Cao S., Ratra B., 2022, *MNRAS*, 513, 5686
- Cao S., Biesiada M., Jackson J., Zheng X., Zhao Y., Zhu Z.-H., 2017, *J. Cosmology Astropart. Phys.*, 2, 012
- Cao S., Ryan J., Ratra B., 2020, *MNRAS*, 497, 3191
- Cao S., Ryan J., Khadka N., Ratra B., 2021a, *MNRAS*, 501, 1520
- Cao S., Ryan J., Ratra B., 2021b, *MNRAS*, 504, 300
- Cao S., Dainotti M., Ratra B., 2022a, preprint, (arXiv:2204.08710)
- Cao S., Ryan J., Ratra B., 2022b, *MNRAS*, 509, 4745
- Cao S., Khadka N., Ratra B., 2022c, *MNRAS*, 510, 2928
- Cao S., Dainotti M., Ratra B., 2022d, *MNRAS*, 512, 439
- Chávez R., Terlevich R., Terlevich E., Bresolin F., Melnick J., Plionis M., Basilakos S., 2014, *MNRAS*, 442, 3565
- Chen G., Ratra B., 2011, *PASP*, 123, 1127
- Chen Y., Ratra B., Biesiada M., Li S., Zhu Z.-H., 2016, *ApJ*, 829, 61
- Coatman L., Hewett P. C., Banerji M., Richards G. T., Hennawi J. F., Prochaska J. X., 2017, *MNRAS*, 465, 2120
- Colgáin E. O., Sheikh-Jabbari M. M., Solomon R., Bargiacchi G., Capozziello S., Dainotti M. G., Stojkovic D., 2022, *Phys. Rev. D*, 106, L041301
- Collin-Souffrin S., Dyson J. E., McDowell J. C., Perry J. J., 1988, *MNRAS*, 232, 539
- Czerny B., Hryniewicz K., 2011, *A&A*, 525, L8
- Czerny B., et al., 2021, *Acta Physica Polonica A*, 139, 389
- D'Agostini G., 2005, preprint, (arXiv:physics/0511182)
- DES Collaboration 2019, *Phys. Rev. D*, 99, 123505
- Dainotti M. G., Nielson V., Sarracino G., Rinaldi E., Nagataki S., Capozziello S., Gnedin O. Y., Bargiacchi G., 2022a, *MNRAS*, 514, 1828
- Dainotti M. G., Bargiacchi G., Lenart A. L., Capozziello S., Ó Colgáin E., Solomon R., Stojkovic D., Sheikh-Jabbari M. M., 2022b, *ApJ*, 931, 106
- De Cicco D., et al., 2022, preprint, (arXiv:2205.12275)
- De Rosa G., et al., 2015, *ApJ*, 806, 128
- de Cruz Perez J., Sola Peracaula J., Gomez-Valent A., Moreno-Pulido C., 2021, preprint, (arXiv:2110.07569)
- Demianski M., Piedipalumbo E., Sawant D., Amati L., 2021, *MNRAS*, 506, 903
- Dhawan S., Alsing J., Vagnozzi S., 2021, *MNRAS*, 506, L1
- Di Valentino E., et al., 2021a, *Classical and Quantum Gravity*, 38, 153001
- Di Valentino E., Melchiorri A., Silk J., 2021b, *ApJ*, 908, L9
- eBOSS Collaboration 2021, *Phys. Rev. D*, 103, 083533
- Eckart A., et al., 2017, *Foundations of Physics*, 47, 553
- Efstathiou G., Gratton S., 2020, *MNRAS*, 496, L91
- Fana Diriras F., et al., 2019, *ApJ*, 887, 13
- Ferland G. J., Done C., Jin C., Landt H., Ward M. J., 2020, *MNRAS*, 494, 5917
- Fonseca Alvarez G., et al., 2020, *ApJ*, 899, 73
- Geng C.-Q., Hsu Y.-T., Lu J.-R., 2022, *ApJ*, 926, 74
- Glanville A., Howlett C., Davis T. M., 2022, preprint, (arXiv:2205.05892)
- González-Morán A. L., et al., 2021, *MNRAS*, 505, 1441
- Grier C. J., et al., 2019, *ApJ*, 887, 38
- Handley W., 2019, *Phys. Rev. D*, 100, 123517
- Homayouni Y., et al., 2020, *ApJ*, 901, 55
- Hoormann J. K., et al., 2019, *MNRAS*, 487, 3650
- Hu J. P., Wang F. Y., Dai Z. G., 2021, *MNRAS*, 507, 730
- Ivezić Z., et al., 2019, *ApJ*, 873, 111
- Jesus J. F., Valentim R., Escobal A. A., Pereira S. H., Benndorf D., 2021, preprint, (arXiv:2112.09722)
- Johnson J. P., Sangwan A., Shankaranarayanan S., 2022, *J. Cosmology Astropart. Phys.*, 2022, 024
- Karas V., Svoboda J., Zajaček M., 2021, in RAGtime: Workshops on black holes and neutron stars. p. E1 (arXiv:1901.06507)
- Kaspi S., Brandt W. N., Maoz D., Netzer H., Schneider D. P., Shemmer O., 2007, *ApJ*, 659, 997
- Kaspi S., Brandt W. N., Maoz D., Netzer H., Schneider D. P., Shemmer O., Grier C. J., 2021, *ApJ*, 915, 129
- Khadka N., Ratra B., 2020a, *MNRAS*, 492, 4456
- Khadka N., Ratra B., 2020b, *MNRAS*, 497, 263
- Khadka N., Ratra B., 2020c, *MNRAS*, 499, 391
- Khadka N., Ratra B., 2021, *MNRAS*, 502, 6140
- Khadka N., Ratra B., 2022, *MNRAS*, 510, 2753
- Khadka N., Yu Z., Zajaček M., Martínez-Aldama M. L., Czerny B., Ratra B., 2021a, *MNRAS*, 508, 4722
- Khadka N., Luongo O., Muccino M., Ratra B., 2021b, *J. Cosmology Astropart. Phys.*, 2021, 042
- Khadka N., Martínez-Aldama M. L., Zajaček M., Czerny B., Ratra B., 2022a, *MNRAS*, 513, 1985
- Khadka N., Zajaček M., Panda S., Martínez-Aldama M. L., Ratra B., 2022b, *MNRAS*, 515, 3729
- KiDS Collaboration 2021, *A&A*, 649, A88
- Kollmeier J. A., et al., 2017, preprint, (arXiv:1711.03234)
- Kovačević A., et al., 2022, The LSST era of supermassive black holes accretion-disk reverberation mapping, *ApJS Focus Issue* (submitted)
- Leizerovich M., Kraisselburd L., Landau S., Scóccola C. G., 2022, *Phys. Rev. D*, 105, 103526
- Lewis A., 2019, preprint, (arXiv:1910.13970)
- Li E.-K., Du M., Xu L., 2020, *MNRAS*, 491, 4960
- Lian Y., Cao S., Biesiada M., Chen Y., Zhang Y., Guo W., 2021, *MNRAS*, 505, 2111
- Liddle A. R., 2007, *MNRAS*, 377, L74
- Lira P., et al., 2018, *ApJ*, 865, 56
- Liu Y., Chen F., Liang N., Yuan Z., Yu H., Wu P., 2022, *ApJ*, 931, 50
- Luongo O., Muccino M., 2021, *Galaxies*, 9, 77
- Luongo O., Muccino M., Colgáin E. O., Sheikh-Jabbari M. M., Yin L., 2022, *Phys. Rev. D*, 105, 103510
- Lusso E., et al., 2020, *A&A*, 642, A150
- Mania D., Ratra B., 2012, *Physics Letters B*, 715, 9
- Martínez-Aldama M. L., del Olmo A., Marziani P., Sulentic J. W., Negrete C. A., Dultzin D., D'Onofrio M., Perea J., 2018, *A&A*, 618, A179
- Martínez-Aldama M. L., Czerny B., Kawka D., Karas V., Panda S., Zajaček M., Życki P. T., 2019, *ApJ*, 883, 170
- Martínez Aldama M. L., Panda S., Czerny B., Zajaček M., LSST AGN SC

- Collaboration 2020a, in *Multifrequency Behaviour of High Energy Cosmic Sources - XIII*. 3-8 June 2019. Palermo. p. 10 ([arXiv: 1910.02725](https://arxiv.org/abs/1910.02725))
- Martínez-Aldama M. L., Zajaček M., Czerny B., Panda S., 2020b, *ApJ*, **903**, 86
- Mehrabi A., et al., 2022, *MNRAS*, **509**, 224
- Mejía-Restrepo J. E., Lira P., Netzer H., Trakhtenbrot B., Capellupo D. M., 2018, *Nature Astronomy*, **2**, 63
- Metzroth K. G., Onken C. A., Peterson B. M., 2006, *ApJ*, **647**, 901
- Mukherjee P., Banerjee N., 2022, *Phys. Rev. D*, **105**, 063516
- Müller A. L., Naddaf M.-H., Zajaček M., Czerny B., Araudo A., Karas V., 2022, *ApJ*, **931**, 39
- Naddaf M. H., Czerny B., 2022, *A&A*, **663**, A77
- Naddaf M.-H., Czerny B., Szczerba R., 2021, *ApJ*, **920**, 30
- Netzer H., 2019, *MNRAS*, **488**, 5185
- Ooba J., Ratra B., Sugiyama N., 2018a, *ApJ*, **864**, 80
- Ooba J., Ratra B., Sugiyama N., 2018b, *ApJ*, **866**, 68
- Ooba J., Ratra B., Sugiyama N., 2018c, *ApJ*, **869**, 34
- Ooba J., Ratra B., Sugiyama N., 2019, *Ap&SS*, **364**, 176
- Panda S., 2022, *Frontiers in Astronomy and Space Sciences*, **9**, 850409
- Panda S., Martínez-Aldama M. L., Zajaček M., 2019a, *Frontiers in Astronomy and Space Sciences*, **6**, 75
- Panda S., Marziani P., Czerny B., 2019b, *ApJ*, **882**, 79
- Park C.-G., Ratra B., 2018, *ApJ*, **868**, 83
- Park C.-G., Ratra B., 2019a, *Ap&SS*, **364**, 82
- Park C.-G., Ratra B., 2019b, *Ap&SS*, **364**, 134
- Park C.-G., Ratra B., 2019c, *ApJ*, **882**, 158
- Park C.-G., Ratra B., 2020, *Phys. Rev. D*, **101**, 083508
- Pavlov A., Westmoreland S., Saaidi K., Ratra B., 2013, *Phys. Rev. D*, **88**, 123513
- Peebles P. J. E., 1984, *ApJ*, **284**, 439
- Peebles P. J. E., Ratra B., 1988, *ApJ*, **325**, L17
- Penton A., et al., 2022, *MNRAS*, **509**, 4008
- Perivolaropoulos L., Skara F., 2022, *New Astron. Rev.*, **95**, 101659
- Peterson B. M., et al., 2005, *ApJ*, **632**, 799
- Peterson B. M., et al., 2006, *ApJ*, **641**, 638
- Planck Collaboration 2020, *A&A*, **641**, A6
- Prince R., et al., 2022, preprint, ([arXiv:2201.11062](https://arxiv.org/abs/2201.11062))
- Rakshit S., 2020, *A&A*, **642**, A59
- Rana A., Jain D., Mahajan S., Mukherjee A., 2017, *J. Cosmology Astropart. Phys.*, **2017**, 028
- Ratra B., Peebles P. J. E., 1988, *Phys. Rev. D*, **37**, 3406
- Renzi F., Hogg N. B., Giarè W., 2022, *Mon. Not. Roy. Astron. Soc.*, **513**, 4004
- Rezaei M., Solà Peracaula J., Malekjani M., 2022, *MNRAS*, **509**, 2593
- Riess A. G., Casertano S., Yuan W., Bowers J. B., Macri L., Zinn J. C., Scolnic D., 2021, *ApJ*, **908**, L6
- Risaliti G., Lusso E., 2015, *ApJ*, **815**, 33
- Risaliti G., Lusso E., 2019, *Nature Astronomy*, **3**, 272
- Ryan J., Chen Y., Ratra B., 2019, *MNRAS*, **488**, 3844
- Scolnic D. M., et al., 2018, *ApJ*, **859**, 101
- Shen Y., et al., 2019, *ApJ*, **883**, L14
- Singh A., Sangwan A., Jassal H. K., 2019, *J. Cosmology Astropart. Phys.*, **2019**, 047
- Sinha S., Banerjee N., 2021, *J. Cosmology Astropart. Phys.*, **2021**, 060
- Solà Peracaula J., Gómez-Valent A., de Cruz Pérez J., 2019, *Physics of the Dark Universe*, **25**, 100311
- Spiegelhalter D., Best N., Carlin B., Van Der Linde A., 2002, *Journal of the Royal Statistical Society. Series B: Statistical Methodology*, **64**, 583
- Starkey D. A., Horne K., Villforth C., 2016, *MNRAS*, **456**, 1960
- Ureña-López L. A., Roy N., 2020, *Phys. Rev. D*, **102**, 063510
- Vagnozzi S., Di Valentino E., Gariazzo S., Melchiorri A., Mena O., Silk J., 2021a, *Physics of the Dark Universe*, **33**, 100851
- Vagnozzi S., Loeb A., Moresco M., 2021b, *ApJ*, **908**, 84
- Wang J. S., Wang F. Y., Cheng K. S., Dai Z. G., 2016, *A&A*, **585**, A68
- Wang F. Y., Hu J. P., Zhang G. Q., Dai Z. G., 2022, *ApJ*, **924**, 97
- Wei J.-J., Melia F., 2022, *ApJ*, **928**, 165
- Xu T., Chen Y., Xu L., Cao S., 2022, *Phys. Dark Univ.*, **36**, 101023
- Yu H., Ratra B., Wang F.-Y., 2018, *ApJ*, **856**, 3
- Zajaček M., Karas V., Eckart A., 2014, *A&A*, **565**, A17
- Zajaček M., Czerny B., Martínez-Aldama M. L., Karas V., 2019, *Astronomische Nachrichten*, **340**, 577
- Zajaček M., et al., 2020a, *ApJ*, **896**, 146
- Zajaček M., Araudo A., Karas V., Czerny B., Eckart A., 2020b, *ApJ*, **903**, 140
- Zajaček M., et al., 2021, *ApJ*, **912**, 10
- Zhai Z., Blanton M., Slosar A., Tinker J., 2017, *ApJ*, **850**, 183
- Zhao D., Xia J.-Q., 2021, *European Physical Journal C*, **81**, 694
- Zheng X., Cao S., Biesiada M., Li X., Liu T., Liu Y., 2021, *Science China Physics, Mechanics, and Astronomy*, **64**, 259511
- Zu Y., Kochanek C. S., Peterson B. M., 2011, *ApJ*, **735**, 80

APPENDIX A: GOLDEN SAMPLE OF C iv QSO DATA

Table A1: Sample of QSOs with a high-quality detection of the C iv time-delay. The sample is based on 38 sources compiled by Kaspi et al. (2021). In the table, we list from the left to the right column: object name, redshift, flux density at 1350 Å, monochromatic luminosity at 1350 Å for the flat Λ CDM model ($H_0 = 70 \text{ km s}^{-1} \text{ Mpc}^{-1}$, $\Omega_{m0} = 0.3$, $\Omega_{\Lambda} = 0.7$), the rest-frame C iv time-lag (in days) determined for all the sources using either the ICCF or the zDCF method (or their combination), and the original reference.

Object	z	$\log(F_{1350}/\text{erg s}^{-1}\text{cm}^{-2})$	$\log(L_{1350}/\text{erg s}^{-1})$	τ (days)	Reference
NGC 4395	0.001064	-11.4848 ± 0.0272	39.9112 ± 0.0272	$0.040^{+0.024}_{-0.018}$	Peterson et al. (2005, 2006)
NGC 3783	0.00973	-9.7341 ± 0.0918	43.5899 ± 0.0918	$3.80^{+1.0}_{-0.9}$	Peterson et al. (2005, 2006)
NGC 7469	0.01632	-9.9973 ± 0.0712	43.7803 ± 0.0712	$2.5^{+0.3}_{-0.2}$	Peterson et al. (2005, 2006)
3C 390.3	0.0561	-10.8036 ± 0.2386	44.0719 ± 0.2386	$35.7^{+11.4}_{-14.6}$	Peterson et al. (2005, 2006)
NGC 4151	0.00332	-9.7544 ± 0.1329	42.6314 ± 0.1329	$3.34^{+0.82}_{-0.77}$	Metzroth et al. (2006)
NGC 5548	0.01676	-10.2111 ± 0.0894	43.5899 ± 0.0894	$4.53^{+0.35}_{-0.34}$	De Rosa et al. (2015)
CTS 286	2.551	-11.6705 ± 0.0719	47.0477 ± 0.0719	459^{+71}_{-92}	Lira et al. (2018)
CTS 406	3.178	-12.0382 ± 0.0402	46.9101 ± 0.0402	98^{+55}_{-74}	Lira et al. (2018)
CTS 564	2.653	-11.7615 ± 0.0664	46.9978 ± 0.0664	115^{+184}_{-29}	Lira et al. (2018)
CTS 650	2.659	-11.8815 ± 0.1068	46.8802 ± 0.1068	162^{+33}_{-10}	Lira et al. (2018)
CTS 953	2.526	-11.7082 ± 0.0868	46.9996 ± 0.0868	73^{+115}_{-58}	Lira et al. (2018)
CTS 1061	3.368	-11.4788 ± 0.0405	47.5299 ± 0.0405	91^{+111}_{-24}	Lira et al. (2018)
J 214355	2.607	-11.7786 ± 0.0485	46.9624 ± 0.0485	136^{+100}_{-90}	Lira et al. (2018)
J 221516	2.709	-11.6263 ± 0.0569	47.1550 ± 0.0569	153^{+91}_{-12}	Lira et al. (2018)
DES J0228-04	1.905	-11.9791 ± 0.0405	46.4298 ± 0.0405	123^{+43}_{-42}	Hoormann et al. (2019)
DES J0033-42	2.593	-12.2248 ± 0.0201	46.5105 ± 0.0201	95^{+16}_{-23}	Hoormann et al. (2019)
RMID 032	1.715	-13.8040 ± 0.0210	44.4928 ± 0.0210	$21.1^{+22.7}_{-8.3}$	Grier et al. (2019)
RMID 052	2.305	-13.1121 ± 0.0021	45.4990 ± 0.0021	$32.6^{+6.9}_{-2.1}$	Grier et al. (2019)
RMID 181	1.675	-13.7265 ± 0.0149	44.5451 ± 0.0149	$102.1^{+26.8}_{-10.0}$	Grier et al. (2019)
RMID 249	1.717	-13.3140 ± 0.0099	44.9841 ± 0.0099	$22.8^{+31.3}_{-11.5}$	Grier et al. (2019)
RMID 256	2.244	-13.4939 ± 0.0030	45.0888 ± 0.0030	$43.1^{+49.0}_{-15.1}$	Grier et al. (2019)
RMID 275	1.577	-12.5961 ± 0.0010	45.6110 ± 0.0010	$76.7^{+10.0}_{-3.9}$	Grier et al. (2019)
RMID 298	1.635	-12.6497 ± 0.0010	45.5960 ± 0.0010	$82.3^{+64.5}_{-24.5}$	Grier et al. (2019)
RMID 312	1.924	-13.3424 ± 0.0040	45.0770 ± 0.0040	$70.9^{+9.6}_{-3.3}$	Grier et al. (2019)
RMID 332	2.581	-13.1795 ± 0.0020	45.5510 ± 0.0020	$83.8^{+23.3}_{-6.5}$	Grier et al. (2019)
RMID 387	2.426	-12.9782 ± 0.0010	45.6870 ± 0.0010	$48.4^{+34.7}_{-10.1}$	Grier et al. (2019)
RMID 401	1.822	-12.8714 ± 0.0030	45.4900 ± 0.0030	$60.6^{+36.7}_{-13.0}$	Grier et al. (2019)
RMID 418	1.418	-13.0533 ± 0.0030	45.0398 ± 0.0030	$58.6^{+51.6}_{-21.3}$	Grier et al. (2019)
RMID 470	1.879	-13.5732 ± 0.0060	44.8210 ± 0.0060	$27.4^{+63.5}_{-22.0}$	Grier et al. (2019)
RMID 527	1.647	-13.4655 ± 0.0030	44.7880 ± 0.0030	$47.3^{+13.3}_{-5.0}$	Grier et al. (2019)
RMID 549	2.275	-13.2283 ± 0.0020	45.3690 ± 0.0020	$68.9^{+31.6}_{-9.6}$	Grier et al. (2019)
RMID 734	2.332	-13.0935 ± 0.0010	45.5299 ± 0.0010	$68.0^{+38.2}_{-11.5}$	Grier et al. (2019)
RMID 363	2.635	-12.2525 ± 0.0206	46.4997 ± 0.0206	$300.4^{+17.1}_{-4.7}$	Shen et al. (2019)
RMID 372	1.745	-12.6952 ± 0.0198	45.6201 ± 0.0198	$67.0^{+20.4}_{-7.4}$	Shen et al. (2019)
RMID 651	1.486	-12.7234 ± 0.0198	45.4200 ± 0.0198	$91.7^{+56.3}_{-22.7}$	Shen et al. (2019)
S5 0836+71	2.172	-11.5354 ± 0.0680	47.0128 ± 0.0680	230^{+91}_{-59}	Kaspi et al. (2021)
SBS 1116+603	2.646	-11.5013 ± 0.0485	47.2553 ± 0.0485	65^{+17}_{-37}	Kaspi et al. (2021)
SBS 1425+606	3.192	-11.2978 ± 0.0356	47.6551 ± 0.0356	285^{+30}_{-53}	Kaspi et al. (2021)

This paper has been typeset from a \LaTeX file prepared by the author.